

DEVELOPMENT OF A SPIN POLARIZED MOLECULAR GENERATOR FOR
SENSITIVITY ENHANCED-REGION 1D NUCLEAR MAGNETIC RESONANCE
SPECTROSCOPY AND IMAGING

By

ANTHONY L. ZOOB

A DISSERTATION PRESENTED TO THE GRADUATE SCHOOL
OF THE UNIVERSITY OF FLORIDA IN PARTIAL FULFILLMENT
OF THE REQUIREMENTS FOR THE DEGREE OF
DOCTOR OF PHILOSOPHY

UNIVERSITY OF FLORIDA

2002

Copyright 2000

by

Anthony J. Zarb

To my Honored Father
Who gave me the ability

To my family
Whose encouragement sustained me.

And to my wife Teresa,
Whose love and support have no limits

ACKNOWLEDGMENTS

The total sum of activity required to complete this work far outweighs my own capacity in complexity and volume. It would not have been possible without the help and support of those around me.

I would first like to thank my family, who have supported me so well through my graduate career. Their unconditional love is essential. They have continuously provided perspective to my work, keeping me ever mindful of its true meaning. Their love and support have been a source of strength for me. The benefit I received from them has no measure. Coming home to the warm love of a beautiful wife and daughter can easily melt the icy emotions of the worst day in the laboratory.

I will forever be indebted to the circle of friends that I have formed since starting graduate school. They have provided encouragement, support, and entertainment, and are the primary reason that my family and I have enjoyed our time in Gainesville.

My time in the lab was made much more enjoyable by the cast of characters that I have shared it with. Their conversations and debates have provided valuable help and guidance in my work, as well as provided an enjoyable work environment.

The funding provided by the National High Magnetic Field Lab (NHMF, NHF), University of Florida, and the Department of Chemistry has been greatly appreciated.

The construction of the pulsed-mr was made possible by the staff of the Chemistry Department Endowment Support Foundation. Jon Kucharski and Todd Poon provided valuable guidance in the design and fabrication of many pulsed-mr components, and Jon Cantow

provided all of the gluing/sewing services for the optical pumping cells and their subsequent repairs.

Many thanks are due to Prof. Steve Blackford and his two post-doctoral associates, Peter Thelwell and Sara Green. They have been a source of great knowledge and direction for the ongoing experiments. Dr. Blackford has also been very generous in the financial support of my projects.

Finally, I would like to thank Prof. Russ Brown for allowing me to participate in the research underway in his lab, and for effectively steering me to the completion of my degree. He found the correct balance between independence and guidance that allowed me to successfully work, learn, and develop as a scientist.

TABLE OF CONTENTS

	PAGE
ACKNOWLEDGMENTS	vi
LIST OF TABLES	viii
LIST OF FIGURES	ix
ABSTRACT	xi
1 INTRODUCTION	1
2 SPIN EXCHANGE OPTICAL PUMPING	4
Optical Pumping	8
Spin Exchange	16
3 IN-SITU SPIN-EXCHANGE OPTICAL PUMPING SYSTEM BASED ON A TITANIUM SAPPHIRE LASER SOURCE	34
Design and Construction	37
Experimental Results and Discussion	39
Conclusions	34
4 DEVELOPMENT OF A SPIN EXCHANGE OPTICAL PUMPING SYSTEM USING A SOLID-STATE LASER DIODE ARRAY	38
Laser System	39
Optical Pumping System	39
Gas Handling System	37
5 PERFORMANCE EVALUATION OF LDA BASED-SPIN EXCHANGE OPTICAL PUMPING SYSTEM	37
Influencing Parameters Factor	37
Cell Temperature	40
Magnetic Field	42
Gas Flow	43
Pumping Cell-Gas Pressure	45
Gas Composition	46
Laser Power	47

Conclusion	68
6. MEASUREMENT OF LASER POLARIZATION ANISOTROPY	70
Introduction	71
Experimental Results and Discussion	76
Instrumentation	76
Thermal Noise-129-Cis Imaging	78
Polarized Noise-129-Cis Imaging	83
Polarized Layout Noise-129 Imaging	86
1D-1D Imaging	75
Final Conclusion	79
PARTS LIST FOR OPTIMIZED POLARIZER	82
LIST OF REFERENCES	84
BIOGRAPHICAL SKETCH	85

LIST OF TABLES

Table	Page
Table 1-1 Thermal polarization of various NMR nuclei at T=300 K and B ₀ =9.4T	4
Table 4-1 Performance of polarized (25%) flow processors using active magnets DNPPT	29
Table 5-1 Experimental values used to calculate ¹³ C hyperpolarization	38
Table 5-2 UP-NMRPL polarizer performance characteristics	49
Table 6-1 Relative signal intensities for protein and serum samples using Hyperion [3.5]	56
Table 6-2 Polarizer operating conditions for polarized serum gel imaging	60
Table 6-3 Polarizer conditions for polarized liquid serum imaging	67
Table 6-4 Polarizer conditions for polarized/ liquid serum imaging	72

LIST OF FIGURES

Figure	Page
Figure 1-1 Information content and sensitivity of common Analytical techniques	4
Figure 2-1 Energy level diagram of rubidium-87	9
Figure 2-2 Excitation of the ^{87}Rb line with an laser light at 780 nm	10
Figure 3-1 Optical pumping cell	17
Figure 3-2 In-situ spin-exchange optical pumping system mounted on-top of superconducting NMR magnet	18
Figure 3-3 In-situ spin-exchange optical pumping system block diagram	19
Figure 3-4 ^{87}Rb polarization enhancement factor versus optical pumping cell temperature	21
Figure 3-5 ^{87}Rb polarization enhancement factor versus $\% \text{N}_2$ in Xe/N_2 gas mixture	22
Figure 3-6 ^{87}Rb polarization enhancement factor versus gas pressure in optical pumping cell	23
Figure 4-1 Optical polarizer and geometry of laser beams for rubidium operation in the optical pumping cell	29
Figure 4-2 CAD drawing of optical pumping system	31
Figure 4-3 Schematic drawing of gas-delivery system	34
Figure 4-4 LP-NMRFL polarized gas generator	35
Figure 5-1 Rubidium vapor absorption of laser light at 780 nm	41
Figure 5-2 Observed ^{87}Rb NMR signal enhancement vs. applied magnetic field in pumping cell	42
Figure 5-3 ^{87}Rb polarization enhancement factor vs a function of the gas flow rate	44
Figure 5-4 ^{87}Rb polarization enhancement factor vs a function of the system pressure	46

Figure 5-5	Linear power vs. NMR signal-enhancement factor	48
Figure 6-1	Basic spin-echo pulse sequence	52
Figure 6-2	Gradient-echo pulse sequence	54
Figure 6-3	Non-slice-selective gradient-echo images of thermally-polarized xenon	60
Figure 6-4	Axial, non-slice-selective, gradient-echo image of polarized xenon gas flow	60
Figure 6-5	NMR spectrum of polarized ^{129}Xe at 1.15K using -2° tip angle	64
Figure 6-6	NMR spectrum of polarized ^{129}Xe at 1.15K using -4.2° tip angle	68
Figure 6-7	Axial, non-slice-selective, gradient-echo image of $\sim 1\%$ polarized liquid xenon	70
Figure 6-8	Capillary phantom sample for MRI contrast and resolution studies	75
Figure 6-9	Axial, non-slice-selective, gradient-echo image of $\sim 35\%$ polarized liquid xenon	76
Figure 6-10	Axial, non-slice-selective, gradient-echo image of water	76
Figure 6-11	Axial, non-slice-selective, gradient-echo image of water	77
Figure 6-12	Axial spin-echo image of water with capillary phantom	78

Abstract of Dissertation Presented to the Graduate School
of the University of Florida in Partial Fulfillment of the
Requirements for the Degree of Doctor of Philosophy

DEVELOPMENT OF A SPIN POLARIZED NUCLEAR GAS GENERATOR FOR
SENSITIVITY ENHANCED X-RAY CT, NUCLEAR MAGNETIC RESONANCE
SPECTROSCOPY AND IMAGING

By

Anthony L. Zink

August, 2002

Chair: Dr. C. E. Sroog
Department: Chemistry

Xenon-129 NMR has long been used as a sensitive surface probe for macromolecular systems such as polymers, proteins, and catalysts. However, the technique is hindered by the low signal intensity of xenon due to its small thermal polarization (approximately 10^{-3} at 3-4 T). The advent of spin-exchange-optical pumping has enabled the production of xenon-129 with a nuclear polarization 4-5 orders of magnitude greater than the Boltzmann equilibrium value. This has led to new NMR applications such as medical imaging of lungs and signal enhancement of other nuclear species by polarization transfer or thermal mixing. The increasing number of NMR and MRI applications requiring large volumes of highly spin polarized xenon-129 or helium-3 gas has placed new demands on spin-exchange-optical pumping (SEOP) systems.

The advent of high-power (>10 W) laser-diode array (LDA) systems with wavelengths in the near-infrared has led to significant advances in the quantity and rate of production of spin-polarized helium-3 and neon-23 gases.

This work reports the development and evaluation of a continuous-flow SCRF system incorporating a 210 W diode array laser system with a 1.7 mm(230-QHz) spectral width. Experimental data detailing the diode array THz nuclear polarizations and bulk magnetization production dependence on various operating parameters such as gas flow rate, gas composition, and magnetic field strength are presented. In addition, this system provides a unique opportunity to study the SCRF performance as a function of laser power up to an unprecedented 210 W. While nuclear polarizations far from the performance benchmarks of polarized noble gas processes, in many applications, it is the bulk magnetization produced per unit time that is of greater relevance.

Finally, results demonstrating the ability to produce neon-23 with a nuclear spin-polarization of $>0.5\%$, as well as the ability to produce spin-polarized neon-23 for imaging and spectroscopy applications, are presented. The ability of the polarizer to produce polarized ^{17}O gas is considered by way of other polarizer currently described in the literature.

CHAPTER 1 INTRODUCTION

Nuclear magnetic resonance (NMR) has become a staple of analytical chemistry because of its ability to provide qualitative and quantitative information about atoms and molecular species. In its simplest form, NMR is the observation of the resonance condition between magnetic nuclei contained in an external magnetic field and an oscillating electromagnetic field.

Nuclei with a spin quantum number $I > 0$ have a magnetic moment. If placed in an external magnetic field, these magnetic nuclei will align, giving a net magnetic moment along the z axis. For an $I = 1/2$ nuclei, this net magnetization can be described by

$$M = \frac{1}{2} N \gamma \hbar P \quad (1.1)$$

where N is the number of nuclei, γ is the gyromagnetic ratio, and P is the polarization of the sample. The polarization of the nuclei is the relative population difference of the two energy states, and is defined as follows:

$$P = \frac{N_u - N_l}{N_u + N_l} \quad (1.2)$$

where N_u is the number of spin up nuclei (lower energy state), and N_l is the number of spin down nuclei. The energy separation between the two states is

$$\Delta E = \gamma \hbar B = \Delta \epsilon_1 \quad (1.3)$$

where B is the magnetic field, and ω_L is the Larmor frequency

$$\omega_L = \frac{\gamma B}{2\pi} \quad (1.4)$$

The resonant frequency can be modified by shielding or deshielding of the applied magnetic field due to the local chemical environment. The shielding field is given by

$$B_{\text{loc}} = -\sigma B_0 \quad (1.5)$$

where σ is the chemical shift parameter. The nucleus experiences the sum of the applied field and the local field such that resonant frequency becomes

$$\omega = \frac{\gamma B_0}{2\pi} (1 - \sigma) \quad (1.6)$$

The ratio of energy states obeys a Boltzmann distribution such that

$$\frac{N_H}{N_L} = e^{-\Delta E/kT} \approx 1 - \frac{\Delta E}{kT} \quad (1.7)$$

where T is the temperature of the system. In the high temperature approximation, where $\Delta E \ll kT$, the nuclear polarization of the sample can be reduced to the following

$$P \approx \frac{\gamma \hbar B}{2kT} \quad (1.8)$$

Applying an rf pulse to the sample causes the magnetization to tip down into the transverse (xy) plane, where it begins to precess at the Larmor frequency. This precessing magnetization can be detected by an NMR coil resulting in a free-induction decay (FID). A Fourier-transformation of the FID results in a frequency plot of the observed NMR signals. The FID decays by two main relaxation mechanisms, T_1 and T_2 . T_1 is the spin-lattice relaxation time constant, which describes how the magnetization relaxes back to its equilibrium value in the B_0 direction. T_2 is the spin-spin relaxation time constant, which describes how the magnetization relaxes to equilibrium in the transverse plane.

NMR of xenon-129 has found considerable use as an indirect probe for surface characterization of heterogeneous materials such as zeolites, molecular sieves, catalysts, clays, and metal oxides.¹⁻³ Investigations of graphite and silica surfaces have been completed as well, although not as readily due to the large amount of signal averaging that is required to produce an adequate NMR signal. Xenon-129 NMR has also been applied to biological systems such as proteins, lipids, and cytoskeletons.⁴⁻⁷

The chemical shift, or chemical shift, of ^{129}Xe is reported on the δ -scale with units of part per million (ppm)

$$\delta_{\text{ppm}} = \frac{\nu - \nu_{\text{ref}}}{\nu_{\text{reference}}} \times 10^6 \quad (1.1)$$

by converting $(\nu_{\text{ref}} - \nu)$ to the units of wave number (cm⁻¹)

Xenon-129 is a popular probe gas for molecular systems due to its great sensitivity in the liquid environment. It has a chemical shift range of greater than 300 ppm when gaseous in a surface, and a total ppm range of 7000.⁸ However, ^{129}Xe suffers from a constant NMR problem, lack of sensitivity. As seen in Figure 1-3, while NMR provides the greatest amount of information relative to common analytical techniques, its sensitivity is among the lowest.

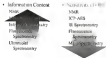


Figure 1-1 Information content and sensitivity of common broadband techniques²

The detected NMR signal voltage is directly proportional to the net magnetization of the nuclei, which is proportional to the number of nuclei and their polarization, as shown in Equation (3-1). The lack of sensitivity in conventional NMR is partly due to the low polarization of the detected nuclei. Table 1-1 shows the thermal equilibrium polarizations of several common NMR nuclei at 300 K and 10 T magnetic field.

Table 1-1 Thermal polarization of common NMR nuclei at $T=300\text{ K}$ and $B=10\text{ T}$

NMR nuclei	Thermal Polarization
^1H	1.3041 $\times 10^{-5}$
^{13}C	1.6141 $\times 10^{-5}$
^{15}N	1.1614 $\times 10^{-5}$

For NMR experiments suffering from low signal to noise, there are three options for increasing the signal-to-noise ratio (S/N): signal averaging, increasing the number of nuclei, and increasing the nuclear polarization.

In zero-dimension Fourier transform NMR, the signal to noise is proportional to the square root of the number of signal averages

$$\frac{S}{R} \propto \sqrt{n} \quad (1.18)$$

where n is the number of signal transients averaged. For example, a four-fold increase in the SNR could be obtained by averaging almost four detection events (FID). Although signal averaging is routinely used, there are practical limits on the improvements that can be gained. Depending on the application, several thousand FID scans are needed to generate an acceptable signal.² For ^{129}Xe , T_1 relaxes from several seconds to tens of minutes, causing experiment times to range from several hours to several days. Waiting several days to collect a usable signal is certainly possible, but not very practical. The need for signal averaging therefore sets practical limits on the type of experiments that can be conducted.

The signal can be increased by increasing the number of detectable nuclei. In the previous state, the amount of ^{129}Xe in the sample can be increased by simply increasing the xenon pressure in the sample tube. However, in samples where high pressures are detrimental, such as in biological systems, the use of high pressures is limited. The sensitivity of experiments involving the detection of nuclei attached onto a surface is limited by the number of surface sites available, so higher pressures would be of no benefit. The use of xenon gas isotopically enriched in the ^{129}Xe isotope is another way to increase the number of detectable nuclei. The natural abundance of the xenon ^{129}Xe isotope is 26.4%. Enrichments of 40% ^{129}Xe are commercially available, but are more costly. The use of isotopically enriched xenon provides a ~three-fold increase in the NMR signal.

The last method of signal enhancement is to maximize the polarization of the nuclei. This can be accomplished by “brute force” methods and non-equilibrium

methods of enhancing the nuclear polarisation. These three methods include increasing the applied magnetic field, or decreasing the temperature of the system. The equilibrium polarisation increases in accordance with Equation (3.8). However, low temperatures are not applicable in experiments performed under ambient or biological conditions.

Furthermore, the spin lattice relaxation times in diamagnetic compounds at cryogenic temperatures can become exceedingly long, prohibiting the nuclear magnetisation from ever reaching thermal equilibrium as a reasonable time scale. Increasing the magnetic field is a more common approach to increase polarisation. This technique is restricted by the practical limits of building large magnet systems. Superconducting magnet systems for NMR can have recently been developed with field strengths of 20.5 T. The National High Magnetic Field Laboratory has recently demonstrated a superconducting and reactive hybrid magnet with a field of 45 T. While this is a major engineering accomplishment, it provides only a factor of 3-4 improvement compared to currently used superconducting magnet fields in the 9-11 T range. The impact for these very high fields is also the potential for higher frequency resonances, along with higher signal to noise.

There are several non-equilibrium methods for generating nuclear polarisation. These enhancement techniques include dynamic nuclear polarisation,^{10,11} gas-byteson induced nuclear polarisation,¹²⁻¹⁴ optical pumping in organic solids¹⁵⁻¹⁷ and semiconductors,^{18,19} and spin-exchange optical pumping of the spin 1/2 noble gases.²⁰⁻²² Spin-exchange optical pumping (SEOP) of the noble gases, proven to be one of the most versatile methods for NMR signal enhancement, has direct applications to ¹²⁹Xe nuclei

Spin-exchange optical pumping, has been used to increase the nuclear polarization of noble gas atoms to near unity. In ^{129}Xe NMR, signal enhancements of $10^3 - 10^4$ are increasingly possible under favorable conditions.²⁰ The ability to produce ^{129}Xe atoms with nuclear polarization values of magnitude greater than thermal equilibrium has not only improved almost all existing ^{129}Xe NMR applications, but also has opened the door to many other applications which were impossible with conventional ^{129}Xe NMR. Most notable is an magnetic resonance imaging of ^{129}Xe and polarization transfer from xenon to other nuclei, such as proteins of gaseous molecules.²¹

The purpose of the research presented here is to construct and demonstrate a spin exchange optical pumping system that is capable of producing ^{129}Xe with the highest possible polarization, and is the greatest possible quantum for use in NMR and MRI applications. This will be accomplished by closely examining the fundamentals of the spin-exchange optical pumping technique, and incorporating them into an experimental device.

CHAPTER 2 SPIN EXCHANGE-OPTICAL PUMPING

Spin-exchange optical pumping (SEOP) is a technique involving the transfer of angular momentum from photons of light to surface spins. It has been primarily used to produce low equilibrium nuclear spin polarizations in helium 3 and xenon 129, although other nuclei have been studied. Production of these spin polarized nuclei has significant importance in physics, chemistry, and medicine. SEOP consists up of two processes: optical pumping and spin-exchange.

Optical Pumping

Optical pumping is the process of using circularly polarized light to create large population imbalances in atomic ground states. The process was first described and experimentally confirmed by Alfred Kastler in the 1950's¹⁸. Kastler was awarded the 1986 Nobel Prize in Physics for the discovery of optical pumping.

Photons have a spin $S_z = \pm 1$, with $m_s = +1$ (σ^+) corresponding to left-circularly polarized light and $m_s = -1$ (σ^-) corresponding to right circularly polarized light. In the absorption of a circularly polarized photon, the conservation of angular momentum requires that the transition of the electrons follow the selection rule ($\Delta m = \pm 1$). In the case of σ^+ light, $\Delta m = +1$, and for σ^- light, $\Delta m = -1$.¹⁹⁻²⁰ While all alkali metals can undergo optical pumping, rubidium has become the metal of choice due to two factors. Firstly, its vapor pressure is such that a high atom density can be generated at temperatures less than 200°C.²¹ Secondly, the rubidium ⁸⁵D line, indicated in Fig. 2.1 for ⁸⁵Rb, occurs at 780

ion, which is in the spectral range of commercially available, tunable, laser such as titanium sapphire and AlGaAs diode lasers.

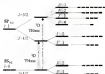


Figure 1-1. Energy level diagram of nitrobenzene-9F showing hyperfine splitting.

In the optical pumping experiment, the nitrobenzene vapor sample is irradiated with laser light tuned to 700 nm causing electron excitation from the S_0 to the lowest S_1 excited state. Absorbing irradiation with σ -light, electrons can relax via the fast $m = 0$ selection rule, shown in Figure 1-2. Excited electrons can then relax, by either fluorescence or non-radiative mechanisms. These transitions can be fast (~ 1), depending on the direction of the excited light. With continued excitation of σ -light, repeated excitation/relaxation cycles result in the electrons being driven or “pumped” into the $m_0 = 1/2$ state, where they become trapped, thus giving the nitrobenzene a net electron polarization. The atoms become trapped in this level because there are no allowed optical transitions out of this state. However, leakage out of this state can occur due to spin relaxation to the ground state.

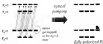


Figure 1-2: Excitation of the 3d line with v-v laser light at $\lambda = 784$ nm resulting in spin-polarized ground state of ^{23}Ne .

In a phenomenon known as relaxation trapping, the excited photons can be absorbed by other rubidium atoms causing optical pumping of the rubidium, which leads to significant depolarization of the rubidium. A quench gas, with neon/gas or hydrogen, can be added to reduce this rubidium trapping. The quench gas provides a non-radiative relaxation pathway for the excited rubidium atoms, thus greatly reducing the rubidium fluorescence. Quench gases such as nitrogen and hydrogen are needed because the excited states transfer energy from the excited electrons to vibrational and rotational degrees of freedom in the diatomic molecules. The translational degrees of freedom return to equilibrium by the transfer of energy to heat.¹⁸

Spin Exchange

Spin-exchange is the transfer of angular momentum from the alkali atoms to nuclear spins via hyperfine exchange. In 1960 Brédas, Carter and Varent, first reported the ability to transfer the electron polarizations of an alkali metal to noble gas nuclei.¹⁹ The impact of this spin exchange on MRF was not fully realized until the early 1980's when Happer and co-workers at Princeton University produced detailed studies of the spin exchange process between optically pumped rubidium and ^{133}Xe .²⁰

When a noble gas atom comes into contact with a polarized Rb atom, there is a hyperfine spin exchange from the rubidium to the noble gas nucleus. At low pressures

the spin exchange is mediated by the formation of a Rb-Xe Van der Waals molecule.

The extended lifetime (several microseconds) of the complex increases the probability that the hyperfine contact interaction will lead to spin-exchange. In a process that competes with spin-exchange, the Rb nuclear magnetism is also transferred to the molecular rotation of the Van der Waals complex. At high pressure (> 1 atm), spin exchange occurs during binary collisions due to the sufficiently limited lifetime of the Van der Waals complexes. Following the transfer of polarization to ^{85}Xe nuclei, rubidium atoms are again eligible for optical absorption and subsequent optical pumping and spin-exchange.

Although the optical pumping spin-exchange mechanism is complex, depending on parameters such as temperature, pressure, magnetic field and pumping cell surface preparation, several research groups have optimized the experimental conditions for the production of hyperpolarized ^{129}Xe and ^{131}Xe .^{12,13} The average ^{129}Xe nuclear polarization at time t after creation is

$$P_{129}(t) = \frac{\Gamma_{\text{ex}}}{\Gamma_{\text{ex}} + k_1 P_{\text{ex}}} P_{\text{ex}} \left(1 - e^{-(\Gamma_{\text{ex}} + k_1) t} \right), \quad (3.1)$$

where Γ_{ex} is the Rb- ^{129}Xe spin exchange rate, k_1 is the relaxation rate of the noble gas nuclei, and P_{ex} is the average electron spin polarization of the rubidium atoms.¹⁴ The average rubidium polarization is given as

$$P_{\text{ex}} = \frac{\Gamma_{\text{op}}}{\Gamma_{\text{op}} + \Gamma_{\text{sd}}}, \quad (3.2)$$

where Γ_{op} is the optical pumping rate of the rubidium electrons, and Γ_{sd} is the spin destruction rate¹⁵ of the rubidium. The Rb- ^{129}Xe spin-exchange rate is defined as

(1) The spin destruction rate is the sum of all mechanisms that contribute to the electron spin relaxation of rubidium.

$$P_{\text{ex}} = c_{\text{ex}}[\delta\hat{I}] \quad (2.3)$$

where c_{ex} is the velocity-averaged binary spin-exchange cross-section and $[\delta\hat{I}]$ is the number density of the Rb atoms, discounted by the temperature-dependent vapor pressure of the rubidium metal.²² The rate of rubidium optical pumping can be described as

$$P_{\text{opt}} = \frac{12I_0}{c} \frac{\Omega_L}{\gamma} I_0, \quad (2.4)$$

where Ω_L is the Raman coefficient of absorption, c is the speed of light, Ω_L is defined as the overlap between the laser lineshape and the atomic frequency response, and I_0 is the laser intensity.²⁴ Equations 2.1 – 2.4 above show how the final ^{87}Rb polarization depends on the the time spent in the optical pumping cell, the temperature of the optical pumping cell, the laser power, and the frequency overlap of the laser output and the Rb -absorption lineshape.

Brown et al. also report a homogeneous magnetic field dependence in the ^{87}Rb polarization and subsequent relaxation.²⁴ The ^{87}Rb relaxation due to wall collisions within the optical cell is dependent on the local magnetic field. A field of greater than 20 gauss is required to make the relaxation rate much less than γ_{H} . It is critical that the applied magnetic field is parallel to the incident laser light. If the laser light is not parallel to the field, the atoms spin will begin to precess around the applied field, preventing any buildup of net atomic polarization.

The ^{13}D line of rubidium occurs at 784 nm. Two laser types are commonly used for continuous-wave excitation of this wavelength. The original RICH experiments were carried out with arc-discharge lamps. More recently, external-cavity lasers, which require

ion-opticon pump laser, have been employed. These lasers produce up to several watts of power and a relatively narrow linewidth. The narrow linewidth is a great advantage due to the Q_2 factor in Equation (2.4). The linewidth of the Colson 100-Watt-ionium supplies have operated without an isolator is ~ 100 MHz, while the Doppler-broadening of the submilliwatt-scope at 10^9 is ~ 250 MHz.²² If tuned to resonance, the laser has 100% overlap with the submilliwatt-scope. The narrow linewidth of the ionium supplies laser allows for the highest published ^{89}Sr polarisation achieved in a prototype cell to be 70%.²³ However, ionium supply lasers have several fundamental and practical disadvantages which limit their utility. Due to limited power output of ionium supply lasers, the pumping cells are limited to a volume of approximately 20 ml, and to pressures less than approximately 300 torr.²⁴ These limitations prevent the possibility of efficient optical pumping under flow conditions, and more only small quantities of atoms can be polarised, the polarised ^{89}Sr NMR applications are limited with such a system. However, the high ^{89}Sr polarisations attainable motivate the development of ionium supply based SHCP systems. A SHCP system based on a ionium supply laser is described in Chapter 3.

The other laser option is the AlGaAs laser diode array (LDA). Extensive commercialisation of AlGaAs LDA's, capable of producing $>100\text{W}$ at 780 nm, have stimulated the use of LDA's in optical pumping experiments. Although there is one single LDA that can produce greater than 50 W of output power, several LDA's can be combined to produce a single 'high-power laser' beam. These lasers have the output power necessary for high volume optical pumping under flow conditions. In a fibre array/packaged EAP system, the output from numerous LDA's are combined via optical

flame and collected to produce a single beam that can be easily collimated and polarized for optical pumping. FAP systems of up to 120 W are currently being used for polarized ^{133}Xe research in color groups.²² According to Equation (2.6), higher power (theoretically) translates to an increased ^{133}Xe nuclear polarization, as well as an increased rate of ^{133}Xe polarization,²³ because higher rubidium atom densities may be used. The construction of a SSCP system using a 250 W LSP, as described in Chapter 4.

The primary disadvantage of the LSP system is the broad spectral output. Line widths of 3.3 nm (543 GHz – 1 Å) TFWs are typical and much greater than the rubidium absorption line.²⁴ Hence, a large fraction of the laser light is off-resonance with the rubidium absorption, yielding a very low Ω_1 value. However, the rubidium 2P absorption can be pressure broadened, causing the absorption linewidth to increase at a rate of 15 GHz/mmHg. For instance, linewidths of 0.3 nm can be achieved when the optical pumping cell is pressurized to 10 mm.²⁵ This allows much more of the laser light to be absorbed, and requires the need for accurate line-tuning of the laser output, an inherent advantage of the broader linewidth.

The pressure broadening of the rubidium line is accomplished by using a buffer gas. Helium rather than argon is employed because it has been found that the depolarizing nature of argon gas reduces the polarization of the rubidium when argon is present in high pressure.²⁶ Helium gas has been found to be the best choice for a buffer gas because it does not interfere with the polarization process.

For production of open polarized ^{133}Xe by the SSCP method, the optical pumping cell must contain a sufficient vapor pressure of rubidium metal, requiring the temperature of the cell be maintained at 120–200 °C. In addition, the cell must contain nitrogen gas to

reduce electron trapping. The Ne^{19}Ne gas mixture is introduced to the pumping cell, and then delivered to the MSH probe via a gas handling system. The pressure and relative concentrations of optical pumping gases is dependent on the laser light source being used and the MSH application for which the polarized ^{19}Ne is being produced.

Based on these principles, two SHCP systems have been developed, and are described in this work. The first uses a titanium sapphire laser system, and the second, a high power LED system.

CHAPTER 3 IN-SITU SPIN EXCHANGE-OPTICAL PUMPING SYSTEM BASED ON A TITANIUM SAPPHIRE LASER SOURCE

The Brown Research Lab has a continuing interest in the application of laser-polarized ^{129}Xe NMR for kinetics and surface studies. Jianhui et al.²⁰ reported the use of laser-polarized ^{129}Xe generated from a titanium sapphire laser based SEOP system for studying the kinetics of gas chloride hydrolysis. In that work, laser-polarized xenon was prepared by a titanium sapphire optical pumping system constructed on a laser table at a remote location. The same system was used to study surface protein binding interactions by laser-polarized ^{129}Xe NMR.²¹ The laser-polarized ^{129}Xe was produced on the SEOP system, and then transferred to the NMR sample tube by cooling the sample tube in liquid nitrogen and condensing the xenon as a solid. The sample tube was warmed to reintroduce the xenon into the gas phase, and then placed in the NMR spectrometer where the spectra were obtained.

To facilitate stopped-flow kinetics, imaging, and studies of rapidly relaxing systems, an in-situ SEOP system was developed which allowed delivery of the polarized gas directly to the sample tube on the NMR probe. This system provides a method for stopped-flow kinetics experiments: maintains the relaxation of the polarized xenon between formation and detection, and allows the sample to be maintained at thermal equilibrium while introducing the xenon gas.

Design and Construction

The HeOP system is similar in design to the one reported by Bush et al.¹⁴⁷ who reported the generation of $\sim 70\%$ polarized ^{133}Xe .¹⁴⁸ The optical pumping cell, shown in Figure 3-1, is a solvent-glass cylinder, 2.5 cm in diameter, and 1.3 cm in length, giving a volume of 7 mL.



Figure 3-1 Optical pumping cell.

The cell contained a small droplet (~ 0.1 g) of rubidium metal. The pumping cell was placed in a PTC wire, which was heated by a stream of nitric oxide passing over a constantly heated rubidium wire. The temperature was controlled using a PID feedback controller (Model CTR0004, Omega Engineering, Stamford, CT). An 8-cm Helmholtz pair, capable of producing a homogeneous magnetic field of 300 G, surrounded the pumping cell and wires. The pumping cell is mounted on a custom-made aluminum platform bolted to the top of the superconducting NMR magnet. The optical pumping cell is directly connected to the NMR sample tube via a glass gas manifold comprised of

(147) This polarisation value is an estimate of the mean polarisation in the pumping cell.

standard metal to metal glass tubing. A dewaxed region was placed in the gas line to allow for the cryogenic condensation of the polarized gases. This provided the ability to remove nitrogen and other gases from the source. This dewaxed region is surrounded by a solenoid coil, which provides the 1 kG magnetic field required to maintain the ^{15}N polarization during the freeze-thaw process.²³ The gas manifold was connected to a vacuum pump, gas monitor, and pressure gauges. The pumping cell and gas manifold were designed to operate at pressures of 1-1000 torr. (The *in-situ* SEOP system is shown in Figure 3-4.)



Figure 3-2: In-situ spin-exchange optical pumping system mounted in a trap of superconducting NMR magnet. A, Optical pumping cell, B, Heater cell, C, Station half of Pennington pair, D, Separator magnet, E, Dewaxed region, F, Manifold, G, Aluminum plate, H, NMR superconducting magnet.

The *in-situ* SEOP system incorporates an Argon-ion laser (Model 1280, Coherent Laser Corp., Santa Clara, CA) pumped resonant copper-ion laser (Coherent Model 6095) tuned to 794 nm to optically pump the rubidium vapor. The laser has a maximum power output of 1.5 W of linear polarized light. The fluxion supply laser is

mounted on a laser table approximately 20 dm from the NMR spectrometer. The laser beam was directed from the laser to the SODF system using a series of mirrors. A quarter wave plate and a series of collimating lenses were then used to produce a beam of circularly polarized light 4 cm in diameter. A block diagram of the setup is shown in Figure 3.3.

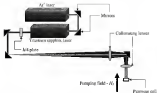


Figure 3.3. In situ spin-exchange optical pumping system block diagram.

Experimental Results and Discussion

Experiments to determine the ^{129}Xe polarization were carried out using the following procedure. The entire optical pumping system, including manifold, was evacuated to a pressure of $<10^{-5}$ torr. The optical pumping cell was then filled with a known pressure of gas from the gas reservoir. The gas reservoir contained a mixture comprised of known partial pressures of nitrogen and natural abundance xenon gas. The valve on the pumping coil was closed, and the rest of the system was evacuated to $<10^{-5}$

ture. The pumping cell was then heated to 100–120°C, while being exposed to a homogeneous magnetic field of 1.6–2.0 T generated by the Heschulte pole. After the temperature of the pumping cell stabilized, the Si/SiO_2 mixture was isolated with 200 ms laser light. After allowing collisions into the optical pumping cell open exchange (0–1 mm), the laser was turned off and the cell was cooled to allow condensation of the nitrogen vapor. The optical pumping cell was then opened to the manifold, allowing the polarized atoms and nitrogen gas mixture to expand into the NMR tube. NMR spectra were acquired immediately after the pressure of the system stabilized, ~3 seconds after the pumping cell was opened. With a known volume and pressure of polarized gas being detected, the polarization was calculated following the method described in Chapter 3. Following NMR detection of the polarized atoms, the laser light was blocked off, the system evacuated, and the procedure repeated.

The optical pumping system was operated under a variety of conditions to determine the set of parameters that provided the highest atom nuclear polarization, as measured by the polarization enhancement factor (ρ'). Temperature and magnetic field of the optical pumping cell were varied, as were the optical pumping time, the percentage of nitrogen in the gas mixture, and the pressure of the gas mixture in the pumping cell.

At some point the optical pumping and open exchange processes will reach a steady state based on the optical pumping cell gas destruction rates of Equations (2.1) and (2.1). After this time, further polarization of the atoms will not occur. Optical pumping times greater than 150 seconds showed no significant improvement in the observed ρ' . Therefore, optical pumping times of 150 s were used for all further experimental studies.

Figure 3-4 shows the dependence of cell temperature on the observed β' . An increase in temperature increases the rubidium atom density due to the temperature dependent vapor pressure of rubidium metal.

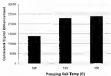


Figure 3-4: ^{85}Rb polarization enhancement factor versus optical pumping cell temperature using an optical pumping time of 150 s, a 30-G magnetic field, and ~200-ppm of a 10% Xe / 90% N_2 gas mixture.

The temperature of the system varied by $\pm 0.1^\circ\text{C}$ from the setpoint, despite the FID temperature controller.

The presence of nitrogen in the optical pumping cell is known to reduce rubidium trapping within the system, thus decreasing the rubidium polarization. Experiments were therefore conducted to determine the effect of concentration of nitrogen on the observed ^{85}Rb polarization enhancement factor. Three gas mixtures were prepared: a pure xenon sample, a 10% Xe / 90% N_2 gas mixture, and a 10% Xe / 90% N_2 gas mixture. The highest β' values obtained with these gas mixtures are shown in Figure 3-5. The gas pressure in the pumping cell was different in each experiment, 46 Torr, 74 Torr, and 130 Torr respectively. This provided roughly equivalent partial pressures of xenon (36, 71, 12

lens) in the optical pumping cell. The values reported in Figure 3-5 represent the best β' values observed with the given gas mixtures.

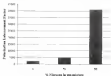


Figure 3-5: ^{133}Xe polarization enhancement factor versus % N_2 in Xe/N_2 gas mixtures, 130 s pumping time, cell temperature = 123 °C, and a 10 G magnetic field

Figure 3-6 shows the β' dependence on the total pressure of the 50% N_2 / 50% N_2 gas mixtures in the optical pumping cell. To understand these results, the effects of relaxation trapping and pressure on the ^{133}Xe polarization need to be considered. Higher total pressures result in more collisions, which reduces relaxation trapping. However, at higher pressures there are more depolarizing spin-spin – spin-lattice collisions that decrease β' . At some pressure the relaxation trapping benefits will reach a maximum, while the depolarization spin-spin interactions will continue to increase.

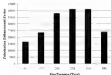


Figure 3.8. ^{85}Kr polarization enhancement factor versus gas pressure in optical pumping cell, 18% Kr / 82% N_2 gas mixture, 150 s pumping time, pumping-cell temperature = 121 °C.

The highest enhancement factor observed was 4000 obtained at a cell temperature of 120 °C, a pumping pressure of 320 torr, a 18-G magnetic field, a pumping time of 150 s, and using the 50% N_2 / 50% Kr gas mixture. The corresponding ^{85}Kr nuclear polarization of 38.6%. Following separation into the detection cell, 3 torr of acetylene was detected. The amount of polarized acetylene produced during each MDP cycle is ~0.3 nM/min. While ρ^2 values of greater than 4×10^3 were observed on several occasions, the day-to-day repeatability was poor. This is probably due to the variation of the optical pumping cell conditions in each experiment, and the stability of the titanium supplies here. Degradation of the cathium metal due to reactions with acetylene, and the pumping cell itself, results in a reduction of the cathium atom density.

The ability to produce highly polarized ^{85}Kr using the in situ setup is greatly dependent on the condition of the cathium within the pumping cell. Following the addition of fresh cathium, the ρ^2 results were not optimal, as the cell needed to be "conditioned". However, after an extended period (several days), the cathium contained

rather the pumping cell would become partially isolated, again resulting in reduced ρ values.

Conclusions

We have demonstrated 30% ^{129}Xe polarization with a SODF system that utilizes a technique superior to ours and allows direct ingestion of the polarized gas into the sample cell for NMR detection. The polarization is not as high as that reported with the SODF system for which this cost was justified⁴². However, the polarization of 70% reported by Roth et al. was not experimentally observed. This value was the calculated outcome of the polarization in the pumping cell based on the observed polarization of C₆D₆ in the NMR spectrometer. The observed polarization was multiplied by a factor of 1.44 to compensate for polarization losses in the transfer from the pumping cell to the sample tube.

Although we used the same gas composition as in the Roth et al. experiments they obtained their best results at a total pressure of 75 torr. Figure 3(d) shows the pressure dependence we observed in our SODF system. In our system a significant decrease in enhancement factor was observed at pressures lower than 200 torr.

The reported technique greatly simplifies the production and detection of polarized ^{129}Xe gas compared to previous methods used in our lab. The in situ optical pumping system was employed in studies of Xe hydrate electronic structure mechanisms and kinetics. However, in order to generate sufficient quantities of polarized ^{129}Xe gas, the system was operated under non-optimal conditions producing ~30% ^{129}Xe polarization.

Reproducibility of the ^{129}Xe polarization was limited. This was in large part due to the modification of the optical pumping cell as directly discussed. Another was reflecting

the repeatability of these experiments was the relative instability of the titanium-sapphire laser. The laser fluctuated in output power and frequency on a day-to-day and even hour-to-hour basis. Other complications with the laser stemmed from beam alignment problems. The laser beam was reflected over a distance of 50 feet, making it difficult to maintain consistent alignment of the beam with the optical pumping cell. The greatest drawback of the titanium-sapphire based SODP system is the small quantity of polarized gas produced which limits the practical applications of polarized ^{13}Xe NMR and MRI.

CHAPTER 4 DEVELOPMENT OF A SPIN-EXCHANGE OPTICAL PUMPING SYSTEM USING A SOLID-STATE LASER DIODE ARRAY

While the SOP system built using the titanium-sapphire laser system produced high ^{129}Xe polarization, it was inadequate for producing the volume of polarized gas needed for the NMR and MRI experiments of interest. As discussed in Chapter 3, there is another type of laser system used in optical pumping, the AlGaAs laser diode array (LDA). Previous work in the polarized gases community has shown the ability of LDA's to generate high volumes of polarized ^{129}Xe as well as more than one decade production. Table 4.1 presents a survey of the ^{129}Xe optical pumping systems described in the current literature according to LDA power, ^{129}Xe nuclear spin polarizations produced, and Xe flow rate. Two relevant criteria by which the performance of a polarized gas generator can be evaluated are the maximum polarization achieved and the nuclear magnetization production rate, a quantity proportional to the product of the nuclear polarization and the Xe flow rate.

Table 4-1: Performance of polarized ^{225}Ac flow generators among active research groups^(a)

Research Group	Location	LDA Power (W)	P (%)	^{225}Ac Flow (nmoles/h)	Polarization Factor	Ref
Agostini (2008)	Lawrence Livermore National Laboratory	50	28	10(20%)	40	64
Cheng (2004)	U. Michigan	30	1.1	-	-	43
Conradi-Kruse (2004)	Washington U.	40	5	1.4(30%)	62	46
Hager Medical Imaging Technologies Inc.	Providence (1997)	100	18	1.3(271%)	272	41
Medford (2000)	U. Virginia	120	3	10.6(20%)	117	44
Tracy (1999)	ORNL (1999)	120	18	12.7(247%)	121	40
Tracy (2001)	Durham, N.C.	100	21	5	61	39
Tracy (2003)	New Mexico Tech.	45	1.5	10(20%)	10.5	51
Tracy (2008)	UC Berkeley	150	10	5(10%)	30	52
Tracy (2011)	Purdue	100	8.5	7(14%)	9	53
Wapner (2004)	ORNL, Canada	30	4	1(20%)	12	54
Wapner (2007)	University of Toronto, France	150	6	1.6(30%)	134	55

Although there are large variations in the reported values of the nuclear polarization and instantaneous production rates, the overall trend suggests that the polarization achieved in previous LDA systems is substantially lower than the value achieved in transient supply systems. However, the use of LDA systems allows for generation of a polarized gas flow, which is not possible with transient supply-based RDP systems using stationary supply sources require several minutes reach a steady state ^{225}Ac polarization. The ideal polarizer would simultaneously achieve both high capacity and the highest possible polarization. Previous work suggests that higher

^(a) While this table may contain double listings for certain flow generators, it presents the best published results obtained from an extensive literature search.

polarization and high flow rates may potentially be obtained by increasing the radiation density and absorbed laser power⁴⁴. However, an experimental investigation to determine if this is true requires a higher-power LDA system than has been previously available.

The National High Magnetic Field Laboratory (NHMFL) and the University of Florida have acquired a 210W LDA system for use in microwave optical pumping. This is apparently the most powerful excitation source have ever constructed at the 780 nm wavelength. A SERF system based on this laser will be able to answer these important questions: Can LDA based polarizers be used to produce high ^{133}Xe polarizations? And, if so, at higher laser power than we do it? Finally, does higher laser power allow higher flow rates to be employed without loss of ^{133}Xe polarization?

The polarizer is modeled after the design reported by Grunberg et al.²⁹ They report the production of 2% polarized atoms, but theorize that ~30% polarization is possible. The SERF system can be broken down into several major components: optical pumping system, gas handling system, and laser light source.

Laser System

The NHMFL UF polarized gas generator incorporates a laser system consisting of seven individual fiber array packages of diode-pumped LDA units (Coherent Laser Corporation, Santa Clara, CA). Each FAP has an optical output of 30 watts that can be independently tuned to 780 nm by diode temperature and current control. The combined optical profile has a line width (FWHM) of 1.4 nm (~400 GHz) at 210 W. The laser output and transmission through the optical pumping cell are continuously monitored with an optical fiber spectrometer (model USA8000, Ocean Optics, Dunedin, FL). As shown in Figure

[44] The flow rates scale with the power density structure of LDA gas cell.

4-1, the individual FAP outputs are combined into a single fiber terminated by a water-cooled output connector. The individual fibers are embedded in a high-thermal-conductivity epoxy and are water-cooled to minimize heating at the connector. The unpolarized beam emerging from the optical fiber enters the optical polarizer where it is collimated before passing through a beam-splitting cube to divide the beam into horizontal and linear polarization components. The vertically polarized beam enters the optical polarizer through a quarter-wave plate. The horizontally polarized beam is reflected by an adjustable mirror and enters through a second quarter-wave plate with the flat surface parallel to the slow axis of the first quarter-wave plate. The mirror mount is adjusted such that the two beams recombine at the pumping cell, which is located at a distance of 10 cm.

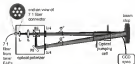


Figure 4-1 Optical polarizer and geometry of laser beams for rubidium excitation in the optical pumping cell. BS-beam splitting cube, L-lens, M-adjustable mirror, 1/4-quarter wave plate, OP cell-optical pumping cell, CCD spec.=crossed-spectra optical spectrometer

This optical polarizer arrangement permits the full power of the laser system to be vertically polarized, despite the output of the fiber system being unpolarized. The transmitted laser power (light not absorbed by the rubidium vapor) is captured in a water-cooled beam stop (Lentek Corporation, Fairfield, NJ).

Optical Pumping System

The cylindrical optical pumping cell is a 12 cm borosilicate glass cylinder with 1 cm diameter optical flats sealed to each end. The internal volume is 296 cm³. Borosilicate glass tube and valves (Chromalox, Waukegan, IL) are attached to the front and rear of the cell allowing gas to flow through the cell (Figure 4-1). The front valve is 3.3 mm O.D. PFA tubing is made using SwagelokTM reducing unions with Teflon liners. The cell now has a 1.3 cm expanded region to accommodate a small quantity (approximately 0.3 g) of rubidium metal.¹⁷ The cell is mounted such that its front window is rotated slightly away from the perpendicular to rotation of the magnet bore frame.



Figure 4-1 CAD drawing of glass optical pumping cell, A: Gas inlet, B: Expanded region for rubidium deposit, C: Pumping cell, D: Gas outlet

Coating the internal surface of the pumping cell with titanium has been shown by Brown et al.¹⁸ to reduce vacuum surface relaxations, thereby improving the ¹³³Xe

(17) Because of the propensity of rubidium with oxygen and water vapor, the rubidium is stored under pumping cell under dry nitrogen atmosphere.

polymerization.¹⁷ A commercially available chlorosulfonate, Surfalol (Pierce Chemical), is most commonly used in root optical pumping cells. The chlorine bonds to the glass surface to form siloxane, and subsequently condenses with surface hydroxyl groups.¹⁸

The optical pumping cell was chemically cleaned with a 7:1 v/v mixture of concentrated sulfuric acid and 30% aqueous solution of hydrogen peroxide. Following rinsing with deionized water, the cell was filled with a hexane solution of Surfalol (0.1 v/v ratio of solution solids). The cell was then allowed to dry *in vacuo* heated to 120 °C. It was then evacuated to 10^{-7} Torr before the rubidium was injected.

Experiments with the Mithril, UV polymerizing-coated and window-optical pumping cells showed a negligible difference in the ability to generate polarized ^{85}Kr gas. There are two explanations for this observation. First, the accommodation coefficient is reduced at high pressures, as the atoms strike almost less frequently with the pumping cell walls, making gas phase relaxations dominant. Second, because the system operates under flow conditions, the atoms atoms spend a limited time (~ 1 s) exposed to the pumping cell, again limiting the wall-induced relaxations. This agrees with the discussion by Brown et al.¹⁹ who show that, at pressures greater than 2 atmospheres, wall induced relaxations no longer dominate the atom relaxation rate.

The pumping cell is enclosed in an oven constructed of aluminum shielding fitted with 20 cm diameter air interfaces covered optical windows at the front and rear. The oven is heated by a forced air resistance filament heater (Chromalox, Model 661-1011), Hansford, MA). The temperature is maintained using a PID feedback controller (Model C98000A, Omega Engineering, Stamford, CT). The oven has a maximum operating temperature of 120 °C, and is stable to ± 1 °C of the request.

When the pumping well is tested, gas passing through the expanded region of the inlet column valve well becomes saturated with rubidium vapor, carrying it into the body of the pumping well. Close inside the pumping well, the rubidium vapor will be optically pumped by the incident laser light. Several techniques suggest using rubidium metal sealed in glass wood¹⁸ or copper wood¹⁹ to increase the surface area of the rubidium metal. Both of these techniques were used, but showed no significant improvement over placing a simple ring of rubidium metal on the expanded region.

A magnetic field is applied to the pumping well by a home built Helmholtz pair. The coils are 40 cm in diameter and are mounted 11 cm apart. Each coil contains 100 turns (~300 feet) of 14 gauge copper magnet wire wrapped on an aluminum spool. The Helmholtz pair are powered by a Sonotek Model SLR 40-20 power supply. The magnet system can generate a 10 cm field of 0.100 G, with a homogeneity of 0.2% of the applied field.



Figure 4-3 Calibration of optical pumping system. A, He-Ne discharge pump; B, aluminum wheels with anti-reflexive windows; and C, laser beam stop; D, optical polarizer; E, circularly polarized laser beam; F, Platform mount.

The entire optical pumping system is mounted on an aluminum frame with castor wheels for transport around the lab. The MCP system is fully enclosed by aluminum shoring, 1/8 inch thick to prevent evolutions of laser light into the laboratory area, and protect against possible glassware failure at high pressures. The aluminum shoring, as well as all interior aluminum parts are painted black to limit reflections of laser light inside the polarizer. The entire SGP system is 5 feet high, 3 feet wide, and 4 feet long.

Gas Handling System

The gas handling system, shown in Figure 4-4, is designed to provide a continuous stream of the polarized ^{23}Ne gas mixture directly to the NMR probe for detection, or to a storage magnet for separation and accumulation of hyperpolarized ^{23}Ne nuclei.

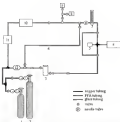


Figure 4-4. Schematic drawing of gas delivery system. 1. Xe cylinder, 2. H₂ cylinder, 3. optical pumping cell, 4. sample line, 5. pressure gauge, 6. sample assembly mounted into box of superconducting magnet, 7. flowmeter, 8. vacuum pump, 9. relief valve, 10. exposure tank, 11. reduction pump, 12. gas purifier.

Tubing for the system is either PFA or copper, and valves and fittings are brass or stainless steel. Stopcocks, valves and fittings were obtained from George Valve and Fitting, Auburn, GA. The valves and flowmeters are purchased from the website of the polaron box. A complete list of commercially available components for the polaron box is included in the Appendix.



Figure 4-5. UF-NMRFL polarized gas generator

Three different gas mixtures were purchased from Spectra Gases (Orlando, FL), each consisting of equal mole percentages of Xe and N₂ at 1, 2, and 10% with the balance made up of helium. The 1% mixture contained xenon with a ¹²⁹Xe isotope enrichment of 90%. The other mixtures contained natural abundance xenon (35–45% ¹²⁹Xe). The output of the storage cylinder is connected to a gas purifier (Model 100, Airmax Inc., San Diego, CA) to reduce the O₂, CO, CO₂, H₂, H₂O, and wet carbon. Hydrocarbon content is less than 1 ppb. The system pressure is monitored using the NMR probe using a Baratron pressure transducer (Model 7214, MKS Instruments, Andover, MA). The polarized ¹²⁹Xe gas mixture is delivered from the pumping cell to the NMR sampling chamber via a 4.7 m length of PFA tubing. The flow rate is controlled and monitored via the valve line by a combination needle valve and variable rate flowmeter (Model 11-02117 OH-Cole-Parmer, Vernon Hills, IL).

After passing through the probe, the gas can either be vented to the atmosphere (in applications where the gas may have become contaminated) or recirculated back to

the pumping cell. In the closed-cycle recirculation mode, flow is generated by a magnetically-coupled gas recirculation pump (Model 1142F, Thomas Ltd., Westborough, MA). For experiments requiring the recirculation of hyperpolarized ^{129}Xe liquid or solid, a stainless steel ballast tank with a volume of 2.5 liters can be inserted into the loop to increase the total volume of the system. The entire gas handling system, including the glass pumping cell and sample tubes, was designed and tested to approximately 10 atm of pressure.

CHAPTER 5 PERFORMANCE EVALUATION OF LDA-BASED SPIN-EXCHANGE OPTICAL PUMPING SYSTEM

The UH-NMR-FL SOSP system was constructed to provide maximum values of all operating parameters that can positively affect the production of laser-polarized ^{129}Xe gas. The pumping cell temperature, pumping field, gas flow, gas pressure, and laser power were systematically varied to determine the values that maximize the observed nuclear polarization-enhancement factor (\mathcal{E}^{N}).

Polarization Enhancement Factor

The figure of merit for a SOSP system has traditionally been the polarization enhancement factor of the polarized ^{129}Xe NMR signal. The ^{129}Xe nuclear polarization enhancement factor, \mathcal{E}^{N} , is defined as the ratio of the laser polarized to the thermal equilibrium (field polarized) ^{129}Xe nuclear polarization

$$\mathcal{E}^{\text{N}} = P_{\text{L}}^{\text{N}} / P_{\text{E}}^{\text{N}} \quad (5.1)$$

The enhancement factor is determined experimentally from the ratio of the NMR signal integrals obtained after Fourier transformation of a single FID recorded from one mole of laser-polarized ^{129}Xe gas, P_{L}^{N} , and thermal equilibrium field polarized gas, P_{E}^{N} , at 300 K, using the same pulse angle for acquisition of each. The nuclear polarization may be deduced from the product of an experimental measurement of \mathcal{E}^{N} and the calculated thermal equilibrium nuclear polarization

$$P_{\text{L}}^{\text{N}} = P_{\text{L}}^{\text{TH}} P_{\text{E}}^{\text{N}} / P_{\text{E}}^{\text{N}} = P_{\text{L}}^{\text{TH}} \mathcal{E}^{\text{N}} \quad (5.2)$$

In the high temperature experiments at 300 K and $P_0 = 0.1$ T,

$$P_0^{(0)} = \rho_0 k_B T / 2\pi l = 4.6 \times 10^{-16} \quad (5.3)$$

The raw NMR signal integrals I^T and $I^{(0)}$ of the laser polarized and thermally polarized reference samples need to be corrected for the number of nuclei of ^{129}Xe and the number of FFCs transmitted ($N_C^{(0)}$ or N_C^T) in each experiment. For example,

$$N_C^{(0)} = I^{(0)} / \alpha^{(0)} N_C^T, \quad (5.4)$$

where $\alpha^{(0)}$ is calculated from the volume ($\pi r_{\text{eff}}^2 l$) (l is the length of the cylindrical detection region of radius r_{eff}) and the pressure $P^{(0)}$ since the ideal gas law holds well under the experimental conditions. Collecting all of these factors, the raw signal integral ratio must be corrected by the ratio in the number of nuclei, the ratio of the fractional isotopic abundance of ^{129}Xe ($f^{(0)} = f^T$), the ratio of the Xe partial pressures, and the ratio of the square of the mean ratio of the sample radii used for the thermal equilibrium and hyperpolarized experiments:

$$r = \frac{I^T}{I^{(0)}} = \frac{N_C^{(0)}}{N_C^T} = \frac{f^{(0)}}{f^T} = \frac{P^{(0)}}{P^T} + \left(\frac{r_{\text{eff}}^{(0)}}{r_{\text{eff}}^T} \right)^2 \quad (5.5)$$

The characteristics of the cooled thermal equilibrium reference sample and of the hyperpolarized sample produced by the JET-PMNP1 polarizer at 4 K are shown where the flow of the pumping gas was stopped for several minutes, are shown in Table 1. The thermal reference sample gas is flame sealed NMR tube containing 5 mmol of neon gas (natural isotopic composition) and 0.2% mol of oxygen to reduce the ^{129}Xe relaxation time to 1.7 s as measured by spin-echo recovery. For improved signal to noise, 64 free

calculus theory were obtained using an acquisition cycle to delay of 30s. Substituting the typical parameters of Table 5-1 into Equation (3-5) yields an enhancement factor $\mathcal{F} = 32,100$ and a polarization of $P = 45.2\%$.

Table 5-1. Experimental values used to calculate ^{129}Xe polarization

Value	Thermal sample	Laser-polarized sample
System pressure	4000 mm	1400 mm
System cycle duration	0.90	0.80
^{129}Xe saturation fraction, f	0.504	0.80
Sample tube ID, r	7.5 mm	3.4 mm
FID accumulation, N_s	40	1
Signal integration, S	1.00	0.40
Enhancement factor, \mathcal{F}		32100
Polarization, P	0.00045 %	45.2 %

The polarization-enhancement factor is an excellent method of qualitatively comparing the ability of a polarizer to produce polarized ^{129}Xe . However, the advent of high volume production polarizers introduces a more quantitative measure of a polarizer's production. The rate of magnetization production can be given as

$$\frac{dM_z}{dt} = \frac{1}{2} \rho_{^{129}\text{Xe}} P_{^{129}\text{Xe}} \frac{dV}{dt} \quad (3-6)$$

where $\rho_{^{129}\text{Xe}}$ is the density of ^{129}Xe , $P_{^{129}\text{Xe}}$ is the ^{129}Xe polarization, and dV/dt is the change in volume with respect to time. At standard temperature and pressure, Equation (3-6) can be rewritten as

$$\frac{dM_z}{dt} = K \times F_{^{129}\text{Xe}} \times \mathcal{F}, \quad (3-7)$$

where K is a constant, and F is the flow rate in standard cubic centimeters per minute (psccm). This can be used to calculate the magnetization production factor

$$\Delta M^* = F_{^{129}\text{Xe}} \times \mathcal{F}, \quad (3-8)$$

with the same of % polarization = 100%. This figure of merit provides a basis for quantitatively comparing polarizers on the ^{133}Xe polarization and the rate at which it is produced.

Cell Temperature

As is evident from Equations (2.1) – (2.4), the rate of ^{133}Xe magnetization production by spin-exchange optical pumping is dependent on the fraction of the laser power absorbed by the vapor. This in turn depends on the rubidium vapor density. The rubidium vapor density increases with temperature and is also a function of the pumping cell. After extended use, the rubidium metal gradually reacts with impurities such as oxygen and water to form oxides. These oxides form solid solutions with the rubidium, lowering the vapor pressure.¹² Although efforts are made to keep the entire optical pumping system clean and free of oxygen, the optical pumping cell needs to be cleaned and refilled with fresh rubidium metal every 3-6 weeks (equivalent to 100 hours of operation). Figure 2-1 shows three least resistant spin-exchange optical pumping cell temperatures for fresh rubidium metal in “conditioned” cells.



Figure 5-1. Rubidium vapor absorption of laser light at 780 nm with a cell pressure 2400 torr

Temperatures that are too high (Figure 5-1, 170 °C) result in a high rubidium vapor density that absorbs all of the 780 nm laser light near the front of the cell. This leaves unpolarized rubidium vapor at the opposite end of the pumping cell, resulting in lower laser excitation and low polarizations. Temperatures that are too low (Figure 5-1, 110 °C) result in a rubidium atom density that is too low to completely absorb all of the available laser light. The optimum temperature (Figure 5-1, 140 °C) produces a rubidium vapor that absorbs nearly all the laser light, yielding uniformly excited rubidium throughout the length of the cell. Depending on the cell conditioning, 140 °C is not always the optimum temperature for optical pumping. To obtain uniform absorption, the cell is continuously monitored using the Ocean Optics spectrometer.

Magnetic Field

The magnetic field applied to the pumping cell serves to keep the least polarized atoms apart during the time they spend in the pumping cell. Figure 5-2 shows the effect of applied magnetic field on the polarization enhancement factor. Each data point is the average value of five spectra. After the magnetic field was altered, the system was allowed to equilibrate for five minutes, and several spectra were acquired to ensure that the polarizer returned to steady state. Error bars shown are ± 1 one standard deviation of the mean.

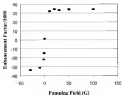


Figure 5-2: Observed ^{133}Xe NMR signal enhancement vs. applied magnetic field to pumping cell. Negative field strength refers to field in opposite direction. Cell pressure = 3400 torr, gas flow = 1.93 mL/min, cell temperature = 150 °C, 1% Xe gas mixture.

The Wheatley pump is operated at 30 G, requiring 2.2 A of current. This provides a high J^2 at a current that does not result in significant heating of the magnet coils.

An interesting phenomenon develops when the pumping field direction is reversed by reversing the direction of the current in the Helderla-pipe. The phase of noise MWR signal is changed by 180 degrees when the pumping field is reversed, indicating an inversion of the ^{129}Xe polarization at high field. This phenomenon is currently being investigated.

Gas Flow

In continuous flow operation mode, the flow rate of the gas mixture determines the residence time of a ^{129}Xe atom in the pumping cell and in the PFA delivery tubing. Figure 1-8 shows a plot of ρ^2 as a function of the pumping gas flow rate (in mL/min) at 4.1 atm total pressure. Each data point is the average value of ten spectra. After the gas flow was altered, the system was allowed to equilibrate for ten minutes, and several spectra were acquired to ensure that the polarization remained at steady state. Error bars shown are at \pm one standard deviation of the mean.

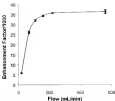


Figure 5.5: ^{129}Xe polarization enhancement factor as a function of the gas flow rate at a system pressure of 4.5 atm (1% ^{129}Xe constant) and a pumping cell temperature of 140 °C and 200 W laser power.

A rapid increase in polarization is observed with increasing flow up to a rate of roughly 100 sccm before leveling off. At flow rates >150 ml/min, the ϵ' remained nearly constant up to 200 ml/min, the highest flow that could be obtained with the gas handling system. Similar results have already been obtained in the 2.7–4.5 atm range. At a flow rate of 150 ml/min, the residence time in the 250-cm² optical pumping cell is approximately 100 μ s, while the transport time in the PFA tubing is roughly 3–6 μ s. This indicates that the residence time is long compared to the ^{129}Xe spin-exchange optical pumping time of τ_{ex}^{-1} , which sets the time-scale for reaching the steady ^{129}Xe polarization according to

$$P_1(t) = P_{\text{St}}(1 - \exp(-t/\tau_{\text{ex}}))^{1/2} \quad (5.9)$$

The data is consistent with the theoretical estimation of $\beta_{\text{eff}}^{-1} = 22 \times$ reported for steady chemical conditions of temperature and gas composition in the literature¹⁸. Since a lower flow rate will only increase the residence time in the pumping cell, the sharp decrease in polarization in the range of 50–100 mTorr must be due to increased relaxation in the PFA tubing during transit through zero field.

Pumping Cell Gas Pressure

The dependence of β' on the pumping gas mixture pressure was observed using two different gas compositions. There are several previous reports indicating the necessity to use pressures in the range of 7–30 atm in order to maximize the optical absorption by means of pressure broadening of the rubidium resonance line^{19,20,21}. As Figure 3-4 demonstrates, the highest β' was achieved, in both the 1% and 2% Xe mixtures, at only 2.5–3 atm. This is probably due to the reduced laser linewidth of 1.4 cm of the LISA employed in our polarizer. In accordance with Equation (3.3), the ability to perform spin-exchange optical pumping at substantially reduced pressure is advantageous since spin destruction of the rubidium is reduced, thereby allowing the rubidium polarization to attain a higher value. The same relaxation rate is also the lowest at this pressure²². The rubidium composition ultimately limits the maximum ¹²⁹Xe nuclear polarization that can be obtained.

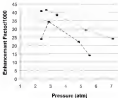


Figure 3-4: ^{129}Xe polarization enhancement factor as a function of the system pressure at a constant flow rate of 150 mL/min. The cell temperature was 140 °C. Circles: 1% Xe mixture at 150 W. Diamonds: 2% Xe mixture at 200 W. Each data point is the average value of five spectra. After the pressure was altered, the system was allowed to equilibrate for ten minutes, and several spectra were acquired to ensure that the polarization returned to steady state. Error bars shown are \pm one standard deviation of the mean.

Gas Composition

The composition of the gas mixture used for optical pumping strongly affects the observed ^{129}Xe polarization. Since the NMR signal is directly proportional to the nuclear magnetization, increasing the polarization by reducing the neon partial pressure may not actually produce a larger NMR signal, because of the decrease in spin-density. While the ^{129}Xe nuclear polarization is greatest with the 1% xenon concentration, certain experiments may require a greater amount of polarized ^{129}Xe , so the optimum gas composition will be application dependent. Table 3-2 shows the dependence of the observed ^{129}Xe nuclear polarization and magnetization production value (MPV) on the

nuclear polarization in the gas mixture. The polarization values shown are not the maximum values achieved, but rather the typical values observed in day-to-day operations of the polarizer. The MPP is taken to be the product of the observed ^{129}Xe polarization, and the flux rate, in scans.

Table 3-3: LPE-NMRPL polarizer performance characteristics

Laser Power (W)	P (%)	Xe/N ₂ /He Composition	Xe Flux Rate (scans)	MPP
200	48	1:1:98	4.86(30%)	192
200	23	2:1:96	7.44(38%)	171
200	12	3:1:97	13.85(34%) ^(a)	373

Laser Power

The ability to perform spin exchange optical pumping with a laser power up to 210 W affords unique opportunity to study the optical power dependence of the ^{129}Xe nuclear polarization. For example, as shown in Figure 3-5, at a pumping cell temperature of 140°C the ^{129}Xe nuclear polarization increases linearly with increasing laser power up to 100 W and then levels off.

(a) This flux rate corresponds to 1.1 hour mode

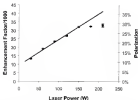


Figure 3-3: Laser power vs. NMR signal enhancement factor and corresponding % ^{13}C nuclear polarization. This data resulted from using the 1% Xe gas mixture at a pressure of 2000-torr, and a pumping cell temperature of 140 °C. The flow rate was 150 mL/min. Each data point is the average value of five spectra. After the laser power was altered, the system was allowed to equilibrate for five minutes, and several spectra were acquired to ensure that the polarizer returned to steady state. Error bars shown are at a one standard deviation of the mean.

This leveling off is attributed to the saturation of the optical transition at the impurities and rubidium density. To avoid this saturation, it is necessary to increase the rubidium density by increasing the cell temperature. The highest ^{13}C nuclear polarization achieved with our polarizer operating in full laser power was observed at 130 °C. However, temperatures above 140 °C proved to be problematic when creating the relatively high densities of rubidium vapor at laser powers in excess of 130 W. Under these conditions, there is substantial heating of the gas mixture due to optical absorption and subsequent excitation and translational energy. Thermal gradients in excess of 30 °C over the 12 cm length of the pumping cell were measured on the outer surface of the

pumping cell. Under these conditions, the temperature can become unstable as this heating results in an increased volatility density that in turn further increases the optical absorption. As this occurs, the front of the cell becomes optically denser, and the beam does not penetrate the vapor near the rear of the cell. Thus, it was found to be imperative to monitor the temperatures at the front and rear windows of the pumping cell with independent thermocouple devices so that large temperature gradients could be avoided at high laser power. The heating effect, thermal gradient, and temperature-control problems made it too difficult to obtain the laser-power dependence at higher temperatures where the optical absorption of the vapor does not saturate.

The data reported in Figure 5-5 is rather misleading, as improvements made to the polarizer after that date has been shown have significantly increased the observed σ^0 . The polarizer is currently able to produce a more flow with 42% polarization. However, the trend seen in Figure 5-5 remains the same, such that the system is still not operating at the optimal volatility vapor density at laser powers greater than 1 MW. Based on the trends seen in Figure 5-3 and the data taken after the polarizer enhancements, a value of 60% axon methyl polarization appears to be possible with this polarizer.

Conclusions

The highest ^{13}C polarization observed in continuous flow mode was 40% using the 1% Xe pumping gas mixture at a Xe flow rate of 4 l/min. A ^{13}C polarization of 40% has been achieved under static conditions. To our knowledge there are the highest levels of ^{13}C polarization to be achieved in an LDA-based ^{13}C polarizer, and furthermore, the MPP also appears to be higher than any other previous literature report of any flow cell. The improved performance is most likely attributed to the high laser

power and narrow laser line width. As discussed above, the reduced linewidth allows a lower pumping pressure to be used.

The ^{133}Xe nuclear polarization obtained with this LISA-based system approaches that of the transverse-sapphire-based polarizer, but the capacity of the LISA system, in terms of the rate of ^{133}Xe magnetization produced, is far greater. The ability to generate quantities of highly polarized ^{133}Xe in excess of 1 L. per-hour will facilitate superior results in both 1D and 2D NMR experiments. Further improvements in performance are anticipated once temperature gradients and temperature control problems are remedied. The ability to achieve the 210 W laser system to achieve even higher polarizations and RPT than reported here will depend on ability to achieve more uniform circulation of the vapor and better temperature control of the pumping cell. One possibility being considered is to split the laser output into two parts and circulate the pumping cell from both the front and rear by two counter-propagating beams of opposite helicity of the circular polarization. Optimization of the pumping cell and laser beam geometry may also mitigate the problems associated with temperature gradients at high laser power.

CHAPTER 6 MRI OF LASER POLARIZED NEON-129

Introduction

Magnetic resonance imaging (MRI) is a 2D or 3D spatial representation of NMR signal intensities. In its most conventional form, it is a mapping of spin density, where the picture element, or pixel, intensity is proportional to the number of nuclei of a specified isotope contained in the volume element, or voxel.³² In clinical settings, MRI of water protons has become one of the most versatile and powerful non-invasive imaging methods.³³

MRI is based on the principle that the Larmor frequency, ω_L , of a nuclear spin is proportional to the local magnetic field it experiences

$$\omega_L = \gamma B_0 \quad (5.1)$$

where γ is the nuclear gyromagnetic ratio and B_0 is the applied magnetic field. If a linear magnetic field gradient is applied across a sample, the Larmor frequency, ω , will be a linear function of the displacement along the gradient axis. Equation (5.1) can be expanded to include a field gradient

$$\omega = \gamma(A_0 + G \cdot r) \quad (5.2)$$

where A_0 and \vec{G} are vectors representing the gradient amplitude and direction with units of field strength (gauss) and length (m G⁻¹, millitesla per meter [mT/m])³⁴ When combined with rf pulses, the application of gradients along different axes results in a frequency or

(32) NMR signal intensity at a voxel also depends on relaxation mechanisms.

phase encoding of the position of the nuclear spins. The sequence of rf pulses, the field gradient pulses, and delays, is referred to as an imaging pulse sequence. A variety of imaging sequences has been developed for encoding spatial information into the nuclear magnetization. Figure 6-1 shows the basic spin echo imaging sequence that is commonly used to generate 2D MR images.

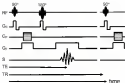


Figure 6-1 Basic spin echo pulse sequence where TE refers to the echo formation time, and TR is the time in which the pulse sequence is repeated.¹⁰⁰

Three linear field gradients are used, one along each of the x , y , and z axes.

These gradients correspond to one or more of the functional gradients that are used to generate an image: slice selection, frequency encoding, and phase encoding. Each are applied during certain portions of the imaging sequence. To select an imaging plane along the z -axis, the slice select gradient, G_z , is applied along the z -axis during the rf excitation pulses. Typically, the excitation pulse is a weak or shaped pulse, and excites only a narrow frequency band corresponding to the resonance condition for spins within a

¹⁰⁰Original sequence adapted from Brown, A. *MRI: Theory, Principles and Applications*, Wiley and Sons, New York, 2000.

specified phase of the sample. A variable phase encoding gradient, G_y , is subsequently applied along the y axis. During this gradient pulse, the single quantum coherence that was excited at a given displacement, x_0 , in the selected direction is phase encoded by

$$\varphi(x) = \varphi(x_0 + G_x \cdot x) \gamma_q \quad [6-3]$$

where γ_q is the pulse length of the phase-encoding gradient. Finally, the frequency encoding gradient, G_z , is applied along the z axis during the detection period. The displacement z_0 along the z axis is proportional to the frequency of the detected transverse magnetization,

$$\omega_0 = \gamma(B_0 + G_z z_0) \quad [6-4]$$

To obtain a complete two-dimensional image in the x - y plane, the pulse sequence is repeated and the NMR signal is collected as a function of the phase encoding gradient strength. For example, if a two dimensional image consisting of 128x64 pixels is to be obtained, the read gradient must be large enough to separate the spins into 128 different observable frequencies, and the sequence is repeated 64 times, each with a different phase gradient strength. The resulting data matrix is a 2D FID which is Fourier transformed in each dimension to yield a 2D frequency plot. Because the observed frequencies are proportional to the position in the sample, this 2D frequency plot represents a spatial image of the sample, where pixel intensity is equivalent to the amplitude of the NMR signal resulting from spins detected within that pixel. In the sequence shown in Figure 6-4, TE is the time allowed for echo formation, and TR is the repetition time, or the time in which the sequence is repeated. Altering TE affects T_2 weighting of the image, while TR affects T_1 weighting.

As in all analytical imaging techniques, there is a constant push to improve the resolution and contrast of MRI. Image resolution is limited by signal intensity and the instrument gradient strength. In clinical imaging, the former is far more limiting than the latter. Contrast is limited by the difference between neighboring spins of density, chemical shift, or relaxation rates.

In clinical practice, portions of free water molecules are imaged. While providing excellent physiological information, there are some tissues that cannot be successfully imaged by proton MRI. In some cases proton MRI provides little contrast within tissues because the concentration, chemical shift, and relaxation times have little variation. For example, the water flow gas spaces of the lung without providing no detectable $^1\text{H}_2\text{O}$ MRI signal. Similarly, the lipid-rich areas of white matter provide little free water to generate MR signals in the brain.⁴⁰ Other MR detectable nuclei occur at such small concentrations that low signal to noise (SNR) values limit their clinical use. Lipid-polarized contrast-129 can be administered to a living human or animal specimen via inhalation or injection.⁴¹ Although these methods yield relatively low in vivo concentrations of contrast (25, 100% signal/enhancement) due to (SOP) prior to administration allows ^{129}Xe images with sufficient SNR for in vivo clinical studies.⁴²

Since the first report of MRI of polarized ^{129}Xe by Albert *et al.* in 1994,⁴³ there has been rapid development in the use of polarized xenon gas MRI in both biological systems,⁴⁴⁻⁴⁶ and materials applications.⁴⁷⁻⁵¹ Polarized ^{129}Xe has been imaged in both humans and guinea pig lungs,⁴⁵ dissolved and imaged in tissue tissues,⁴⁶ and used as a contrast agent in angiography.⁵²

The application of polarized gases to human clinical MRI has prompted the formation of Molecular Imaging Technologies Inc. (MITI) a commercial venture dedicated to producing polarized gas generators for medical research. MITI holds several patents regarding polarized gas generators and applications of polarized gas MRI.¹¹ With both industrial and academic interest, the field of polarized gas imaging is rapidly growing in both a research and commercial clinical diagnostic device.

The development of polarized gas imaging is far from exhausted, new applications to both materials and medical imaging are abundant. While the U¹³C-MRI polarizer provides the ability to participate in the use of research, the interest to develop new techniques for polarized ¹²⁹Xe imaging has prompted our investigation of the feasibility of polarized liquid xenon imaging. MRI of liquid polarized Xe has been previously reported by several research groups,¹²⁻¹⁵ with initial MRI results reported by Tseng et al.¹² However, the full potential of polarized liquid Xe-MRI, in terms of maximum available signal, resolution and contrast, has yet to be fully explored.

Polarized liquid xenon is of significant interest because it provides a magnetization source that can, in principle, be much greater than that of water protons, even at the highest clinically magnetic fields. In MRI applications maximum signal translates into higher resolution and/or less signal averaging. The intensity of a MRI voxel can be described by:

$$I \propto P \propto \rho \sin(\alpha) \propto \rho \quad (0.1)$$

(a) MITI was founded in 1998 and in 2000 was purchased by American Fluids, an international corporation specializing in medical diagnostics. American Fluids has also acquired the patents controlling commercial applications of polarized gas generators and imaging.

where P is the polarization of the nuclei, n is the nuclear number density (spin-density), μ is the nuclear magnetic moment, α is the flip angle of the NMR excitation pulse and ω_1 is the Larmor frequency.¹⁸ Table 6-1 shows the relative signal intensities for protons of water and xylene samples (optical densities) at 9.4 Tesla. The signal intensity for protons in water has been normalized to 1.00 to facilitate comparison. Density of water gas and liquid is taken as 1 atmosphere and 298 K and 1.03 K, respectively. Experiment: time (hours:minutes:seconds) is the time required to obtain a 256x256 image (not 1/s using the given experimental conditions).

Table 6-1: Relative signal intensities for protons and xylene samples using Equation 16.2.

Sample	H ₂ O (l)	Xylen	Polarized H ₂ O(g)	Polarized H ₂ O(l)
Polarization	3.26×10^{-2}	4.64×10^{-2}	0.36	0.39
N (10^{23} nucleus/cm ³)	6580	3.79	2.76	398
μ (J/T ² (BT))	1.441	6.248	0.383	0.343
α (°)	90	90	4.3	4.5
ω_1 (MHz)	400.1	710.8	110.6	730.4
Normalized signal	1.00	1.04×10^{-2}	3.07×10^{-3}	1.98
Experiment Time	1:25:30		8:08:00	0:00:00

Table 6-1 demonstrates the possibility of obtaining high-resolution images

without signal averaging that have twice the signal of the best possible proton images.

Best time is realized in the case of polarized gases because there is no need to wait for T_1 relaxation in the sample. In the interest of shortening experiment times, closed ¹H₂O images are not acquired under the best conditions. Compared to standard images, polarized liquid xylene NMR under these conditions, has a 130-fold increase in signal with equivalent scan times.

Best of all, with the first in-spect NMR of polarized liquid xylene.¹⁹ Using the polarized xylene flow generator described by Debyeys et al.²⁰ approximately one gram of

nitrogen was collected and isolated in a cryogen trap. The nitrogen solid was transferred to a sample cell and warmed to 200 K, where the associated nitrogen vapor pressure is five atmospheres. Polarization of the liquid nitrogen was reported to be 6%. The T_1 of liquid nitrogen was observed to be 25 minutes at 140 G and 18 minutes at 0.5 G. It has also been demonstrated that polarized liquid nitrogen may be used as a solvent for organic solid-state molecules.¹¹ Cross polarization from the polar unit nitrogen liquid to the solids resulted in signal enhancements of 45 and 70 fold for the ^1H and ^{13}C NMR signals, respectively.

In 1990 Tseng et al. reported magnetic resonance imaging of laser-polarized liquid nitrogen.¹² An MRI study of interactions between the liquid and gaseous state of polarized nitrox was subsequently published.¹³ In these experiments, nitrogen gas was polarized to 3% using the standard SERF technique, and then condensed and isolated in a small Pyrex cell. This cell was kept at 100 K, where the vapor pressure of nitrogen is 1 atmosphere. Approximately 50 mm³ of polarized liquid nitrogen was generated with this technique. The image resolution limit of polarized liquid nitrogen at 100 K was calculated to be $\sim 10 \mu\text{m}^2$ with no signal averaging, and a gradient strength of 100 G/cm.¹² Potential applications of polarized liquid nitrogen as a magnetization source for MRI include the study of density equilibration in critical fluids, MRI investigations of two-phase liquid/gas phenomena, and probing porous media microstructures using low field MRI.¹⁴

Low-field NMR and MRI is limited in thermally polarized samples, as the polarization is proportional to the applied magnetic field. This is why recent efforts have been made to develop larger magnets as a method to maximize SNR of NMR.¹⁵ However, when using hyperpolarized magnetization sources such as polarized nitrogen gas and liquid, large magnetic fields are not required to generate the nuclear polarization. Tseng et al.¹²

reported lower polarized ^{129}Xe NMR in a field of 21G. At these low fields, magnetic field anisotropy does no longer limit the resolution of NMR.²⁰

Lamoreaux *et al.*²¹ and Hader *et al.*²² have reported modest steady polarized supercritical xenon. In both of these studies, ^{129}Xe gas was polarized in RFDP polarizers and then isolated in small volume NMR tubes. Experiments were carried out near room temperature and at pressures of 80–110 atmospheres, well above the critical point of xenon. Hader *et al.* were able to demonstrate signal enhancements of 148 relative to the equilibrium signal. Lamoreaux *et al.* generated supercritical xenon with a polarization of 5%, and using it as a solvent, observed cross-polarization from the xenon to protons of organic solute molecules.

Given the demonstrated utility of polarized liquid xenon, we performed experiments with the LF-NMFL polarizer to demonstrate the ability to generate sizable amounts (5.2 mL) of polarized liquid xenon for NMR and NMR experiments with higher ^{129}Xe polarization than previously reported. A novel procedure was developed in which the entire polarization, collection, and detection process occurs in a closed loop environment. This approach has the advantage that the polarized liquid xenon can be recirculated and repolarized for use in subsequent experiments. The xenon is transported directly into the bore of the superconducting magnet where it is cryogenically frozen out of the helium-ethanol xenon gas mixture using the variable temperature control of the Bruker NMR probe. This collection method reduces polarization loss due to T_1 relaxation because the entire process occurs in the high magnetic field of the NMR magnet.²³

The purpose of the project was to collect high resolution images of polarized liquid xenon and compare those images to equivalent ^3He images. The ability of the LF-NMRPL polarizer to produce higher ^{129}Xe polarization at higher flow rates than previously reported allows the production of sufficient quantities of liquid xenon with a nuclear polarization of 80%. This method for the production of polarized liquid xenon is much simpler than methods previously reported, and allows for rapid repetition of polarized liquid xenon NMR and MRI experiments.

Experimental Results and Discussion

Instrumentation

All xenon imaging experiments were performed using the Bruker 10mm high resolution probe in conjunction with an imaging gradient-coast (Model 40H), Bruker Inc. Billerica, MA. These gradients have a maximum strength of 1000 mT/m in the x, y and z-direction. For imaging experiments, the detection coil shield of the 10mm probe used for spectroscopy experiments was replaced with a shimless shield. The standard coil shield can develop eddy currents when the gradients switch on and off. These currents can cause distortions in the local magnetic field that lead to image distortions. The shimless shield, because it is non-conducting, does not cause eddy currents. The gradients were cooled with recirculating chilled water at all times to prevent overheating of the gradients during gas imaging, and to prevent freezing during liquid xenon imaging. Images were acquired and processed using Bruker's Paravision 2.6.1 software.

Thermal Xenon-129 Gas Imaging

To prepare for polarized xenon imaging, the spectrometer was first set up to image thermally polarized xenon. This provided a method of optimizing many of the spectrometer and imaging sequence parameters. To test the capability to image xenon,

Images of a thermal standard gas sample containing 1.0 atmosphere of xenon gas (natural abundance) and 0.16 atm of oxygen gas were acquired. The O_2 was added to reduce the T_1 relaxation time of the ^{133}Xe to 1.5 seconds (as compared to $T_1 \sim 10$ minutes for pure Xe gas), as measured by cross-polar recovery. The relaxation to T_1 involves relatively rapid signal averaging, which is not practical otherwise. A 90° pulse calibration was made by incrementing the rf increment-pulse length, while keeping the pulse power constant. A plot of signal intensity vs. pulse length results in a sinusoidal plot with the first maximum corresponding to the 90° pulse length.

Images were collected using the gradient-echo pulse sequence (GEFT) shown in Figure 6-2. This pulse sequence was dc field gradients to flatten the slices, differing from the spin-echo sequence which uses an rf pulse. The GEFT sequence is advantageous for polarized gas MRI because it allows the use of a small tip-angle pulse to create transient magnetization at the beginning of the sequence. The use of a small tip-angle pulse allows only a small fraction of the total ^{133}Xe magnetization to be used for each increment, as the phase-matched gradients. For a small enough tip angle, the magnitude of the transient magnetization remains nearly constant over the course of the 2D acquisition, and the entire image can be collected using a single batch of polarized xenon.

While a small tip-angle initial pulse could in principle also be implemented in a spin-echo imaging sequence, such an experiment would require a highly homogeneous and accurate 90° pulse. Modulation or spread of inhomogeneity in the 180° rf pulse leads to an accelerated-depletion of the ^{133}Xe magnetization.

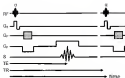


Figure 8.2 Gradient-echo pulse sequence where α denotes the flip angle¹

A major drawback of the GRE sequence becomes more evident at high magnetic fields (>1 T). Spatial variation of the magnetic susceptibility within the volume is for imaging produces distortions in the local magnetic field that are proportional to the applied magnetic field. As a result, the magnetic field gradient in the vicinity of an abrupt change in the magnetic susceptibility is distorted, and the linear relationship between Larmor frequency and displacement no longer holds. In the spin-echo sequence, the 180° pulse causes the transverse magnetization to refocus even in the presence of these field distortions. Thus, the spin-echo sequence produces images that are free of susceptibility artifacts. However, in sequences using gradient echoes, such as GRE and EPI (echo planar imaging sequence), distortions due to susceptibility variations are magnified and are proportional to the B_0 field. This leads to large artifacts, which decrease resolution and image quality.

(1) Pulse sequence adapted from Brown, R. MRI Basic Principles and Applications, Wiley and Sons, New York, 1996.

Calibration of the vortex gas thermal reference 90° head of pulse was completed, as was the T_1 measurement. The T_1 relaxation time was 1.7 s, which requires a recycle delay (TR) time of 10 seconds to assure complete T_1 relaxation. Despite the high power of proton in the thermal reference sample, the image had to be signal averaged 312 times in order to obtain a reasonable S/N. Images obtained from the vortex gas reference sample are shown in Figure 6-3. The values for in-plane resolution are obtained by Equation (6-4):

$$\Delta = \frac{FOV}{\sqrt{MDS}} \quad (6-4)$$

where FOV is the field of view, and MDS is the matrix dimension of the image

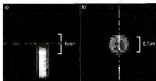


Figure 6-3. Two slices taken from gradient echo images of thermally polarized proton. (a) Sagittal image, 64x32 sampling matrix, FOV=4.0 cm, 90° flip angle, 312 signal averages, TR=5 s, TE=12 ms, in-plane resolutions=0.7 mm x 1.4 mm, experimental time=22:43:20. (b) Axial image, 64x32 sampling matrix, FOV=2.0 cm, 90° flip angle, 683 signal averages, TR=5 s, TE=12 ms, in-plane resolutions=0.4 mm x 0.8 mm, experimental time=21:44:20.

The image in Figure 6-3(b) shows the bottom of the sample tube, but does not show the top. The top of the image is not the end of the sample, but rather the end of the detection coils. The TR of the both images is only 5 s instead of the 10 s delay required

for complete T_1 relaxation. The shortest TR was used as an effort to keep the experiment times within practical limits.

Three images of the xenon gas reference demonstrate the ability of the NMR spectrometer to acquire xenon images. In spite of the long acquisition times, the signal-to-noise ratio (SNR) and resolution are comparatively low. Both of these values could be increased with additional signal averaging. However, this becomes impractical due to extended experiment times, which has led to the motivation of developing more polarized imaging methods.

Polarized Xenon-129 Gas Imaging

Following the successful demonstration of xenon imaging of the thermal standard, imaging experiments were performed using polarized xenon gas. The polarizer was operated in the recirculation configuration under the operating conditions listed in Table 4-2.

Table 4-2 Polarizer operating conditions for polarized xenon gas imaging

Variable	Value
Laser Power	180W
Pumping Cell Temperature	160°C
Pumping Cell Field	30G
Gas Pressure	1800 psig
Gas Flow Rate	145 mL/min
Gas Mixture	75% ^{129}Xe /25% ^{136}Xe
Polarization	~13%

Prior to acquisition of the ^{129}Xe image, NMR spectra of the flowing xenon gas were obtained for estimating the ^{129}Xe nuclear polarization according to Equation (2.9). After confirming that the polarizer was producing ^{129}Xe at the desired level of polarization, axial images of the gas, similar to Figure 4-3b, were obtained.

Figure 5-4 presents axial gradient echo images of the polarized ^{129}Xe gas.

Typical polarized gas images require the use of small tip-angles so as to only sample portions of the excitation magnetization. This is necessary because the bulk magnetizations will not regenerate due to T_1 relaxation. Because the sample was a constant flow of polarized xenon gas, the sample within the rf coil was constantly being refreshed. This allowed for the use of 90° pulses. TE was set to 200 ms so that the sample cell had ample time to refill with freshly polarized ^{129}Xe gas.

The phase shift of these images is due to the flow displacement during the echo time of the pulse sequence. Because imaging techniques are highly dependent on the position of the nuclei, the echo is attenuated due to the net displacement that occurs between the rf excitation pulse and the echo formation gradient. The gas flow rate through the NMR coil was ~ 10 cm/s. The effect of flow is evident by the narrowed signal seen in the walls of the NMR tube in both Figures 5-4a and b. This is presumably due to a flow relaxation upon the walls due to gas-wall interactions.



Figure 6-4. Axial ${}^{13}\text{C}$ cross-polarization/magic-angle spinning image of polymerized monomer in flow cell. (a) Single acquisition, FID, $\text{FOV} = 2.8\text{ cm}$, 90° tip angle, single FID, $\text{TR} = 500\text{ ms}$, $\text{TE} = 7\text{ ms}$, in plane resolution 0.8 mm , experiment time = 4.00 s. (b) Single acquisition, FID, $\text{FOV} = 2.8\text{ cm}$, 90° tip angle, 128 signal averages, $\text{TR} = 500\text{ ms}$, $\text{TE} = 7\text{ ms}$, in plane resolution 0.3 mm , experiment time = 1.08 s.

Flow conditions would not be appropriate in applications where the highest possible resolution is desired. However, several applications exist where a gas flow is beneficial or even required, such as velocity imaging of gas through porous materials.²⁰ While the images presented in Figure 6-4 do not exhibit high resolution, they do demonstrate the ability to collect images of polymerized monomer gas in a flow mode of operation. Despite the poor resolution caused by flow, these experiments demonstrate the feasibility to acquire single FID ${}^{13}\text{C}$ images with adequate SNR (Figure 6-4a). Averaging 128 signal transients improved the SNR, but also lengthened the experiment time considerably (Figure 6-4b). Compared to the thermal monomer gas images in Figure 6-3, which required 22.4 hours to complete, the images in Figure 6-4 have comparable SNR and resolution, yet took 12 s to acquire.

Polarized Liquid Xenon-ED Imaging

Liquid xenon was generated by collecting the xenon as a solid in the NMR sample tube, isolating the sample assembly from the polarizer, and raising the sample temperature to a value greater than the melting point of xenon. The melting point of xenon is 161.8, and the boiling point is 166.1 K at a pressure of one atmosphere. For liquid xenon to form, the partial pressure of xenon gas in the sample assembly must exceed the vapor pressure of the liquid, which is linearly dependent on temperature (e.g., 6.75 atm at 164.8 K and 3.0 atm at 160.8 K). If the vapor pressure is not exceeded, the solid xenon will simply sublimate into the gas phase when warmed.

When operating under recirculating conditions, the total amount of Xe in the pumping cell and delivery tubing is relatively small. To increase the amount of xenon available for liquidation, a 2.2 L reservoir tank was inserted into the polarizer recirculation system. This increased the total volume of the system from 0.4 liters to 2.4 liters. Operation under recirculating conditions is often preferable because of the reduction in impurities introduced into the system, and because a negligible amount of the $\text{Xe}/\text{H}_2/\text{He}$ gas mixture is lost in each experiment. Recirculation of the gas mixture is therefore highly economical and extends the working lifetime of the optical pumping cell.

Polarized solid xenon was generated by operating the polarizer in the recirculating mode under the conditions listed in Table 6-3. At these flow rates, it takes 16 minutes for the gas to be recirculated.

Table 4.3: Polymag conditions for polarized liquid xenon samples

Variable	Value
Laser Power	210 W
Pumping Cell Temperature	140 °C
Pumping Cell Field	20-0
Gas Pressure	2300 bar
Gas Flow Rate	160 ml/min
Gas Monitor	21620/1520 ₂ /1000 bar
Xe 125 polarization	-10%

Prior to cooling the probe to condense the polarized Xe, several 1D-MAS spectra were acquired of the polarized ^{129}Xe gas to ensure that the polarizer was generating polarized xenon gas as a stable source. These spectra were also used to calculate the nuclear polarization of the ^{129}Xe gas. The sample tube was then cooled to 115 K using the Bruker variable temperature system. During the low temperature (-119°C) run, water was circulated through the imaging gradient coil assembly to keep it warm, thus preventing the gradients coils from being damaged.

The collection of liquid-polarized solid xenon was monitored by observation of a broad ^{129}Xe MAS peak at 200 ppm as seen in Figure 4-3.

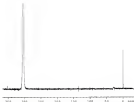


Figure 4-5 NMR spectrum of polarized ^{133}Xe at 155K, using $\sim 3^\circ$ tip angle. Peak at 0 ppm corresponds to polarized $^{133}\text{Xe(g)}$ and broad peak at 244 ppm is $^{133}\text{Xe(s)}$

To avoid destroying the polarization of the xenon solid, a small tip angle ($\sim 3^\circ$) is used. The solid ^{133}Xe signal is merely a qualitative measure of collection, not a quantitative one, because the xenon can condense in areas of the NMR sample tube that are not within the NMR coil detection region. The amount of polarized xenon that could be condensed was also limited by solid xenon freezing in the $1/16"$ ID-PFA tube that delivers the gas mixture into the cold NMR tube. The collection of xenon was halted when the onset of a blockage caused the flow rate to drop below 100 mL/min. Flow rates lower than 100 mL/min result in reduced ^{133}Xe polarization as shown in Figure 4-3.

Collection is halted by isolating the sample assembly from the rest of the polarizer by switching the 3-way valves shown in Figure 4-5. This allows the polarizer to continue processing, while experiments are carried out on the collected polarized xenon. To produce liquid xenon, the sample temperature was then raised to 170-180 K,

cooling the solid xenon to melt into the liquid state. The pressure of the sample was 2.0 \pm 0.1 atmosphere. This phase change is easily observed through NMR, as liquid xenon exhibits a sharp peak at \sim 250 ppm at that temperature (Figure 6-6).

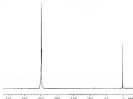


Figure 6-6 NMR spectrum of polarized ^{133}Xe at 101K, using -4.5° tip angle. Peak at 0 ppm corresponds to polarized $^{133}\text{Xe(g)}$ and peak at 250 ppm is $^{133}\text{Xe(l)}$

In cases where a blockage resulted in an insufficient volume of liquid xenon, additional xenon could be subsequently condensed from the polarizer because the blockage is eliminated during the liquefaction. The temperature of the sample tube is again reduced to 113 K, and the sample assembly is reexposed to the polarizer gas flow for enhanced xenon collection. Reduced gas flow did not occur during the second freezing cycle.

Following the collection of xenon solid and the generation of xenon liquid, QNP images were acquired using 4.5° tip angle pulses. There is four images could be obtained before the magnetization of the polarized liquid xenon was depleted. The first image

image was acquired at high resolution to take advantage of the high magnetization that is usually present. Lower resolution images were subsequently recorded to estimate the volume of liquid produced and to experiment with variations of the pulse sequence. Axial and sagittal images of prepared areas were collected.



Figure 6-7: Axial view, slice selective, gradient echo image of $\sim 12\%$ polarized liquid xenon, 128x128 imaging matrix. FOV = 3.0 mm, -4° flip angle. TR = 150 ms, TE = 14 ms, in phase resolution = 60 μ m, experiment time = 0.80 s.

Figure 6-7 shows an axial view of polarized liquid xenon. The cause of the ringing distortion on the outer edges is not completely known, but is most likely volume averaging due to the non-linear behavior of pulses used as the image acquisition. Volume averaging of the liquid xenon resonances, as well as the imperfections of the NMR tube, can result in signal intensity variations near the outside edge of the image. Field inhomogeneities may also contribute to the appearance of rings around the sample.

The artifact appearing as a vertical line in the middle of the image is due to small errors in the computer generated baseline correction of the NMR signal. It appears in nearly all of the images in this study. Although computer-aided correction factors can be

applied to eliminate this artifact, all images are reported as they were originally obtained (with no post processing).

When images with sufficient SNR could no longer be obtained, the NMR tube was heated to -30°C to reposition the liquid meniscus, and the 3-way isolation valve was opened to transfer the meniscus into the polarizer. The gas mixture in the polarizer was allowed to circulate for ~ 10 minutes to allow nitrogen time for the pump to run. The concentration of polarized ^{13}C was measured by periodic 1D NMR spectra. After a steady state production level was reached, the combination of polarized meniscus into the NMR probe was repeated.

Figure 4-7 not only demonstrates the ability to collect polarized liquid meniscus for imaging studies, but also provides some limitations to the collection method. The flow problems limit the amount of meniscus that can be collected. On average, $\sim 20\%$ of the meniscus contained in the polarizer syringe was collected by cooling the sample region. This suggests that a smaller amount of polarized liquid meniscus could be generated using the 2% $\text{Xe}/2\% \text{N}_2/98\% \text{He}$ gas mixture if the collection point could be optimized. This would also increase the polarization of the liquid meniscus, as the 2% gas mixture has been shown to yield steady state polarization of the 2% mixture (Table 5-1).

In an effort to produce liquid meniscus with a higher magnetization, another set of experiments was conducted using the 2% $\text{Xe}/2\% \text{N}_2/98\% \text{He}$ gas mixture. Tests with this gas mixture showed that the solid meniscus observed to form almost solely in the $\sim 1\text{cm}$ diameter FFA tube rather than at the bottom of the NMR tube as desired. This resulted in an increased gas flow during the meniscus freezing process. When the sample was removed to liquefy the meniscus, a large portion of the liquid remained inside the tube

and did not flow to the bottom of the sample tube where it could be detected by NMR. In an effort to concentrate liquid azote from the FFA tube and collect it in the bottom of the NMR tube, the collection procedure was slightly modified. Following the water temperature at 300 K, the exit valve on the sample assembly was opened for about one second. The resulting pressure drop pulled the liquid azote out of the FFA tube and into the bottom of the sample tube. The valve is only left opened for ~ one second. This collection method produced 0.2 mL of detectable liquid azote.

Longer experiments using the 7% gas mixture were conducted with the polarizer operating under the following conditions:

Table 1-4 Polarizer conditions for polarized liquid azote regions

Variable	Value
Laser Power	100 W
Pumping Cell Temperature	140 °C
Pumping Cell Field	30 G
Gas Pressure	1200 torr
Gas Flow Rate	700 mL/min
Gas Mixture	7%N ₂ /75% ¹⁵ N ₂ / 18%O ₂
N ₂ gas polarizers	~20%

Even under increased flow rates, high polarization in the azote gas was observed. At the higher flow rate the gas recirculation time in the polarizer is 3 minutes. Solid polarized azote was allowed to condense for ~10 minutes. During this time, the flow would typically drop from 700 mL/min to 200 mL/min. Because the flow remained at such a high value, there was no need for the flow from system to generate a stable volume of polarized liquid azote. Following collection of the polarized liquid azote, images of the sample were acquired. As before, these images were typically acquired on each sample of polarized liquid azote before allowing the liquid azote to evaporate and

be recycled. Using this method, ~60% of the serum in the system was collected as a liquid for imaging studies.

To investigate image contrast and resolution properties of polarized serum imaging, a simple phantom sample was fabricated for MRI experiments. Capillary tubes of varying diameters and wall thicknesses were inserted into the NMR tube. An axial view of the phantom is illustrated in Figure 6-4.



Figure 6-4: Capillary phantom sample for MRI contrast and resolution studies

Images of both polarized liquid serum were obtained, as were images of polarized liquid serum in the phantom sample.

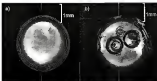


Figure 6-9: Axial view along x-axis, gradient echo image of $\sim 20\%$ polarized liquid xenon, of 12h12f imaging matrix: FOV= 5.0mm, -4.2° tip angle, TE=150ms, TR=15ms, in plane resolution=80 μm , experimental time=0.002s, SNR=18. b) sagittal phantom image, 20h20f imaging matrix: FOV= 5.0mm, -4.2° tip angle, TE=150ms, TR=24.5ms, in plane resolution=80 μm , experimental time=0.010s, SNR=17.

Figure 6-9a shows the bulk polarized liquid xenon generated from the 2% ^{85}Kr / 2% ^{87}Kr / 96% ^{86}Kr gas mixture. The ringing effect, discussed previously is more apparent than in Figure 6-7. The SNR is also greater than in Figure 6-7, due to the increased polarization of the collected liquid xenon.

Figure 6-9b shows the image collected of polarized liquid xenon in the sample sub-cooled glass wall fused silica capillary phantom as described in Figure 6-3. The wall thickness of the fused silica capillary (40 μm) is clearly visible demonstrating that the observed image resolution is similar to that of that of the collected radiation.

Although the outer edge distortions seem to be decreased, there is a significant amount of distortion in this image. This can be attributed to two main causes. The first is the (horizontal) field inhomogeneities caused by the differing magnetic field susceptibility of the materials in the sample. These effects are reduced in the images of the bulk liquid

noise because there is less interaction between materials of differing susceptibility. The second, and more significant source of distortion, is the volume averaging effects caused by the non-phase-selective rf pulses. Because block rf pulses (also known as hard or square pulses) are being used, the slice selection is not accurate, and there is considerable excitation of the entire liquid water sample. This causes signals from a range of z-displacements to be superimposed at the read stage rather than a selective slice. Gradient slice selection can be achieved by using non-shaped rf pulses.

Edge enhancement, similar to what was seen in the polarized gas images, were also seen in the bulk liquid images. This is due to well restricted diffusion of the liquid. Despite these distortions, the NMR of the sample is excellent, and the phantom capillaries are clearly visible.

³H₂O Imaging

To assess the potential utility of polarized gas and liquid ¹²⁹Xe imaging, it is useful to acquire the polarized ¹²⁹Xe images with proton images of liquid water acquired under the similar experimental conditions. Proton images were acquired on a 1 L mL sample of deoxygenated water, which was placed in a glass NMR tube (5.4 mm ID, 1.9 mm OD). This is the same NMR tube used for the polarized liquid water studies described in the preceding section.

In preparation for imaging experiments, the T₁ of the water sample was measured using the standard method of inversion recovery, and a 90° pulse length calibration was performed. The 90° pulse length calibration was determined by measuring the rf excitation pulse length, while keeping the pulse power constant. A plot of signal

minutely versus-pulse length results in a sinusoidal plot, with the first maximum taken to be the 90° pulse length.

To allow for comparison components with the polarized cross images, $^2\text{H}_2\text{O}$ images were taken using the same pulse sequence parameters (e.g., pulse sequence, tip angle, echo time, etc.) as were used for the polarized/liquid cross images. $^2\text{H}_2\text{O}$ images of the phantom sample were also recorded using the same NMR parameters as the liquid cross images.

Figure 4-18 shows the images of the water sample acquired using the same NMR conditions as those used to generate the images in Figure 4-9.

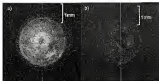


Figure 4-18. A 2D, non slice-selective, gradient echo image of water with: a) 128x128 imaging matrix, $\text{FOV}=3.0\text{ cm}$, -4.3° tip angle, $\text{TR}=1.20\text{ sec}$, $\text{TE}=0.5\text{ sec}$, in plane resolution $=40\text{ }\mu\text{m}$, experiment time $=0.0020$, $\text{SNR}=0.5$, b) capillary phantom image, 256×150 imaging matrix, $\text{FOV}=3.0\text{ cm}$, -4.3° tip angle, $\text{TR}=1.70\text{ sec}$, $\text{TE}=0.5\text{ sec}$, in plane resolution $=20\text{ }\mu\text{m}$, experiment time $=0.0105$, $\text{SNR}=1.6$.

Figure 4-18a presents an image of a bulk water sample taken with a -4.3° tip angle. The artifacts from possible volume averaging are present in this image, but are reduced due to the overall reduction in signal. Although a signal is obviously present, the

image quality is poor due to the low SNR. The calculated SNR of Figure 6-10b is 3.4 and the image is barely recognizable from the noise.

To determine the best SNR possible with the water sample, the images of Figure 6-10 were repeated using 90° flip angles and full T_1 relaxation between pulses. The results is observation of the bulk signal that can be observed from the magnetization of water. The resulting images are shown in Figure 6-11.

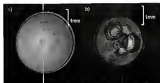


Figure 6-11: (a) Axial, non-oblique reflector-gradients echo image of water; (b) 120x120 imaging matrix, FOV= 5.0 cm, 90° flip angle, TR=50 s, TE=50 ms, in phase resolution=40 μ m, experimental time=0.42 s; SNR=103; (c) sagittal phantom image, 256x128 imaging matrix, FOV= 5.0 cm, 90° flip angle, TR=50 s, TE=50 ms, in phase resolution=20 μ m, experimental time=1.25 s; SNR=39.

Figure 6-11a presents an image of the bulk water sample. The volume average artifacts are less recognizable in this image but still present. In Figure 6-11b, volume averaging artifacts and the magnetic susceptibility distortions are severe. While the image exhibits a good SNR, it is difficult to discern the true structure of the phantom. The experimental times of these images are much longer than in the polarized liquid tensor images.

The comparison between the $^1\text{H}_2\text{O}$ and ^{13}C Ac samples is not exactly quantitative because proton and carbon-12 signals were acquired using different receiver channels and amplifiers of the Fourier spectrometer, and different TMRB levels of the probe. Despite these differences, a semi-quantitative comparison can be made between the ability to collect signals of these two nuclei.

A significant difference exists between the polarized liquid carbon images and the water images taken under the same low flip-angle pulse sequence. Despite using a -4.5° flip angle, the carbon images show an easily observable signal, while in the water images, the signal is barely recognizable. While volume averaging and magnetic susceptibility artifacts are evident in the carbon images, there is not enough signal to know if they are present in the water images.

For the bulk water sample, the image acquired using a 10° pulse is superior to the liquid carbon image in both SNR and magnetic susceptibility artifacts. However, in the phantom sample, the polarized liquid carbon image has an equivalent SNR and maintains a higher level of image clarity due to the reduction in magnetic susceptibility artifacts for the lower γ nucleus. The exposure time of the water images is also 83 times longer than that of the polarized liquid carbon image for the phantom sample.

In clinical imaging of $^1\text{H}_2\text{O}$ samples, spin-echo imaging sequences are typically used. Absolute SNR values are often less of a concern than imaging time, so the TR (repetition time) is set to maximize the overall exposure time while providing sufficient image contrast. The advantage of the spin-echo technique is that susceptibility artifacts due to spin dephasing caused by local field inhomogeneities are refocused by the 180° rf pulse. Water images of the phantom sample acquired with a spin-echo pulse

spectroscopy experiments can be routinely generated in less than thirty minutes. The ability to generate flux volume and polarization of liquid nuclei is directly related to the overall performance of the polarizer. This polarizer is able to produce polarized nuclei, give nuclei and polarizations more before possible, allowing the rapid accumulation of solid polarized nuclei. The rate at which the nuclei can be accumulated is critical, as polarization is being lost to T_1 during the collection process. The polarized liquid nuclei can be generated with the sample cell remaining part of the polarizer, allowing for quick repetition of reproducible experiments. This has never been demonstrated in previously reported polarized liquid nuclei experiments.

The comparison between the $^1\text{H}_2\text{O}$ and liquid nuclei images is the most significant aspect of this work. It demonstrates in a practical application how the magnetization of polarized liquid nuclei is greater than the magnetization of water. It also demonstrates how the higher magnetization source can be used to generate high resolution images without the need for signal averaging, resulting in short imaging times.

The full width of polarized liquid nuclei may never be reached at high field because of magnetic susceptibility effects. Since magnetic susceptibility scales with the square of the applied field, low field imaging systems demonstrate a dramatic decrease in magnetic susceptibility. High field systems are used to increase the equilibrium nuclear polarization as mentioned previously. Because the polarization of the lower-polarized nuclei is not dependent on the applied magnetic field, large high-field superconducting magnets are not necessary to generate usable signals. This makes it possible to perform high resolution imaging experiments with benchtop, low field NMR systems using

gradient echo sequences. These systems are much less expensive to purchase and maintain than traditional, high-field, superconducting magnet systems.

Pulse-width at high field should focus on developing spin echo pulse sequences with precise 180° refocusing pulses to fully exploit the high magnetization of polarized liquid nuclei for imaging studies. However, working at high field, even with gradient echo sequences, provides advantages and opportunities for MRS and MRS spectroscopy not possible at low fields. Chemical-shift-selected imaging is only possible at high fields because at lower fields the frequency separation is too narrow. The T_1 of nuclei is also greater at higher fields, which is advantageous for the MRS and MRS experiments, as more time is available to acquire a signal before significant relaxation occurs.

Apart from the spectrometers, there are many areas of future work to pursue with the NMRPL, perhaps with respect to polarized nuclei imaging. In the completed experiments, the collection time of the solid nuclei was limited to ~ 30 minutes to keep the total experiment time within a reasonable practical limit. However, longer collection times could be achieved enabling the production of a greater volume of polarized nuclei liquid and gas. It is unknown how long solid nuclei can be collected before T_1 relaxation becomes limiting on the total magnetization being collected. The sample cell could also be designed to allow for more efficient collection of polarized solid nuclei.

The imaging experiments described here are simply opening the door to future work, merely demonstrating what is more possible with a high-power, lower-field NMR system.

APPENDIX **PARTS LIST FOR GT-NEMFL POLARIZER**

A table of all commercially available components used in the construction of the GT-NEMFL polarizer described in Chapter 4 is given below.

Vendor	Part Description	Part number
Chromalox	1/20-Rosemount	
	Male connection	CG-170-08
	Female connection	CG-172-08
	Cap	CG-182-08
	Flange	CG-184-08
	O-ring	CG-385-12
	1" window	CG-186-06
	90 degree rotating valve	CG-262-07
Mohawk-Cut	PFA tubing 1/8" ID	31608C31
	PFA tubing 1/4" ID	31608C33
	PFA tubing 3/8" ID	31608C35
Cole Parmer	15mm flow meter	F-82M7-IT
	15mm flow meter	1402212-06
Omega Engineering	Thermocouple	SAJ-E
	Thermocouple main controller	SNP-K-MP
	Thermocouple wire	EXTT-K-24-25
Accurate Temperature Controls	Convectional Metal shell air heater	SH-18211

Vendor	Part Description	Part number
Matheson-Gas Products	High-purity dual stage brass regulator	330C-BB3
MBE Instruments	Random transducer Power supply/ reader Cable	TC1A14TEBA2FA PDR D-1 C7000-2 10
Jaco Valves and Fitting	Brass 1/8" valve	B-48E
	Brass 1/8" tee	B-400-1
	PFA 1/8" tee	PFA-400-2
	Brass 1/8" orifice valve	B-400
	PFA 1/8" union	PFA-400-6
	PFA 1/8" valve	PFA-48754
	Brass 1/8" needle valve	B-284-NV
	PFA 1/8" tube - 1/8" NPT adapter	PFA-430-0-0
	PFA 1/8" tube - 1/8" NPT adapter	PFA-430-1-0
	Stainless steel 1/8" tee	SS-400-0
	Stainless steel 1/8" - 1/8" reducer	SS-400-0-0
	Stainless steel 1/8" - 1/8" reducer B E	SS-400-0-40T
	PFA 1/8" union	PFA-430-6
	Brass edge/side check valve	B-4CTA2-DS-3
	Brass 1/8" tube - 1/8" NPT adapter	B-4-TA-1/4
	Brass 1/8" BH union	B-400-01
	Brass 1/8" - 1/8" matching BH union	B-400-01-2
	PFA 1/8" BH union	PFA-430-61
	Brass 1/8" tube adapter	B-4-MC A-400
	Brass 1/8" matching valve	B-384
	Brass 1/8" 3 way valve	B-40000
KENTHE Corporation	Leak beam damp	AED-AC
Agmox, Inc	Low flow gas purifier	Model 38E
CNI Leak Corporation	AIR control modules	WG-PW-3057-0V 800
TDI Solutions	Thermal Gas Entry Pump	TH28

LIST OF REFERENCES

1. Tinkley, V., Smith, M., Robinson, H. *Colloids and Surfaces A* 1999, 73, 249-254
2. Cho, S. I., Ahn, W. I., Hong, S., Ryoo, R. *J Phys Chem* 1996, 100, 5095-5097
3. Rappaport, J., Ruckelsh, C., Tan, T. *J Chem Soc Faraday Trans 1* 1983, 84, 3775
4. Brown, C., Statham, V., Webster, E., Murgison, J., Collins, A., Gama, R., Boney, K., Gaffney, R. *J Am Chem Soc* 1999, 121, 9378-9377
5. Barth, E., Lohmer, M., Ryoo, S., Ohniger, R., Kresse, J. *J Mag Res B* 1998, 128, 154-160
6. Bruner, E. *Magnetic Resonance in Chemistry* 1998, 11, 814-823
7. Durr, H.C. *Anal Chem* 1984, 56, 741a
8. Jankov, F., Thomas, W. *Macromolecules* 1998, 31, 7044-7053
9. Brown, C., Weidkamp, D. P. *J Am Chem Soc* 1997, 119, 3347
10. Farns, C., Hall, D., Garlin, G., Ison, S., Griffin, R., *J Chem Phys* 1981, 74, 6723-6724
11. Brown, C., Weidkamp, D., *Phys Rev Lett* 1996, 77, 3645
12. Dardelt, S., Gough, C., *Prog Nucl Mag Res Spectrosc* 1999, 34, 71
13. Polunov, T., McDermott, A., *J Phys Chem* 1999, 103, 524
14. Tinkley, E., Takagishi, T., Teras, T. *Chem Phys Lett* 2001, 342, 166
15. AJ. Emswari and V.J. Salovey, *ICTP Lett* 1978, 11, 179
16. Brown, S., Tycko, R., Pfeiffer, L., West, K., *Phys Rev Lett* 1990, 65, 1368
17. Brown, C., *Solid State NMR*, 1998, 11, 11
18. Happer, W., *Rev Mod Phys* 1973, 44, 169

- 19 Kallury, B., Long, H., Murreman, T., Gaudenzi, P., Brown, L., Pines, A. *Phys Rev Lett* **1994**, *54*, 364
- 20 Rath, U., Hof, T., Schmidt, J., Fels, D., Jeschke, H., *Applied Physics B* **1998**, *67*, 81-87
- 21 Louden, C., Bostwick, P., Verbeke, J., Dawson, R., *Physical Science* **2004**, *30*, 762-770
- 22 Happer, W., *Rev Mod Phys* **1973**, *45*, 169-230
- 23 Murreman, T., *A Spectrometer For Optical Pumping and Zeeman* **1993**
- 24 Saut, B., *The Physics of Laser-Atom Interactions*, Cambridge University Press, New York, **1997**
- 25 Happer, W., Walker, T. *Rev Mod Phys* **1993**, *65*, 629-642
- 26 Appelt, K., Danzberg, A., Bräunke, C., Kretsch, M., Young, A., Happer, W. *Phys Rev A* **1998**, *58*, 1412-1429
- 27 Bandaru, M., Carver, T., Yaman, C. *Phys Rev Lett* **1998**, *81*, 373
- 28 Chmurgalski, W., Hübner, G., Lorenzen, W., Swenson, D., Lorenz, B. *Phys Rev A* **1995**, *52*, 4642-4651
- 29 Kallberg, S., Anderson, L., Walker, T. *Phys Rev Lett* **1998**, *80*, 3312-3315
- 30 Kretsch, M., Idman, R., Cina, G. *Phys Rev A* **1997**, *56*, 4565-4570
- 31 Dreifuss, S., Cina, G., Idman, R., Isner, K., Walker, K., Happer, W. *Appl Phys Lett* **1996**, *69*, 1648-1650
- 32 Brown, M., Chapp, T., Coulter, K., Walsh, E., Swenson, S. *Rev Sci Instr* **1995**, *76*, 1546-1552
- 33 Augustin, M., Zinn, K. *Molecular Physics* **1994**, *89*, 773-792
- 34 Brown, M., Chapp, T., Coulter, K., Walsh, E., Swenson, S. *Rev Sci Instr* **1996**, *76*, 1546-1552
- 35 Phillips, D., Wong, G., Kim, D., Simon, R., Walmsworth, R., *Rev Sci Instr* **1995**, *76*, 2526-2529
- 36 Rath, U., Hof, T., Schmidt, J., Fels, D., Jeschke, H. *Appl Phys B - Lasers and Optics* **1998**, *68*, 83-87
- 37 Seydoux, R., Pines, A., Haskin, M., Berman, J. *J Phys Chem B* **1999**, *103*, 8629-8637

- 38 Cummings, W., Hunter, G., Lawrence, W., Swenson, D., Lewis, D. *Phys. Rev. A* **1988**, *37*, 4512-4520
- 39 Ramdas, M., Mann, E., Carr, G. *Phys. Rev. A* **1987**, *36*, 4568-4578
- 40 Storch, V., Lohg, F., Bowen, C., *J. Phys. Chem. B* **2001**, *105*, 2844-2851
- 41 Bowen, C., Storch, V., Wehner, C., Blauders, F., Collins, A., Collins, S., Solovy, K., Gollery, B., *J. Am. Chem. Soc.* **1999**, *121*, 9379-9377
- 42 Roth, U., Heil, T., Schmidt, F., Fick, D., Jentsch, W. *Appl. Phys. B - Lasers and Optics* **1999**, *68*, 31-37
- 43 Grotke, M., Carr, G., Deslages, D., Fox, D., Rappert, W., Sauer, B. *Phys. Rev. Lett.* **1993**, *70*, 448-450
- 44 Shah, N., Tinner, U., Wegmann, H., Halling, H., Zoller, K., Appelt, S., *ADMP. Journal* **2000**, *17*, 214-219
- 45 Webb, B., Clapp, T., Coates, R., Bates, M., Swenson, S., Agnewall, S., *Radi. Isot. and Meas. J* **1998**, *467*, 481-485
- 46 Lennards, J., Sauer, B., Carroll, M., *Chem. Phys. Lett.* **2000**, *321*, 358-364
- 47 Fitzgerald, E., Sauer, B., Rappert, W., *Chem. Phys. Lett.* **1998**, *294*, 17-21
- 48 Rappert, K., Bruderman, S., Fitzgerald, E., Gollery, B., Magill, D., J., *ADMP. Journal* **2000**, *17*, 220-223
- 49 Maier, H., Chavira, M., Chan, S., Deslages, B., Richard, L., Wehner, C., Johnson, G. *Mag. der Med.* **1995**, *47*, 9558-9561
- 50 MTH Corp HG 1600 Xa Polarize Spectrometer, Magnetic Imaging Technologies, Inc., 1200 Mountain Parkway, Suite 173, Durham, NC 27713
- 51 Karlier, J., Sore, B., Surber, E., Calozet, J., Tonnas, A., Nagg, J., Potrich, T., *J. Mag. Res.* **2000**, *147*, 361-365
- 52 Macmillan, T., Legris, J., Swenson, S., Callender, S., Collins, A., Swenson, F., Kuntz, L., Farn, A., *J. Phys. Chem. A* **2000**, *104*, 11663-11670
- 53 Sauer, B., Jentsch, W., MacMillan, E., Krugger, K., Rallory, D., *J. Phys. Chem. B* **2001**, *105*, 1402-1401
- 54 Moudoukoudi, L., Long, S., Ratchell, C., Seward, B., Rappert, W., Repmanstein, J., *J. Mag. Res.* **2000**, *147*, 372-377
- 55 Eubank, G., unpublished results

- 36 Drobny, B., Coss, G., Mann, E., Sauer, K., Weber, K., Happer, W., *Appl Phys Lett* **1996**, *69*, 1668-1670.
- 37 Drees, S., Long, S., Moshinskaya, I., Baichle, C., Rappenstein, I., Renard, B., Sempé, G., *Euro J. Appl Phys* **2000**, *33*, 8013-8017.
- 38 Drees, S., Long, S., Moshinskaya, I., Baichle, C., Rappenstein, I., Renard, B., Sempé, G., *J Appl Phys* **1999**, *85*, 6540-6542.
- 39 Seydoux, E., Fourn, A., Hader, M., Kasser, I., *J Phys Chem B* **1999**, *103*, 4429-4437.
- 40 B. Drobny, G. Coss, E. Mann, K. Sauer, K. Weber, W. Happer, *Appl Phys Lett* **1996**, *69*, 1669.
- 41 Smith, J., Smith, J., Kuegel, K., Markhamer, F., Rader, D., *J Phys Chem B* **2000**, *104*, 1412-1421.
- 42 Seydoux, E., Fourn, A., Hader, M., Kasser, I., *J Phys. Chem. B* **1999**, *103*, 4629-4637.
- 43 Chopp, T., Swanson, S., *Medical Imaging With Polarized Gauss*, University of Michigan, 2000.
- 44 Brown, A., *MRM Basic Principles and Applications*, Wiley and Sons, New York, 1999.
- 45 Albert, M. S., Balciunas, D., *Nucl. Instr. and Meth. In Phys. Res. A* **1998**, *402*, 440-453.
- 46 Lewis, C., Popen, G., Leach, M., Balciunas, A., *MMR Forum* **2000**, *33*, 155-169.
- 47 Albert, M. S., Coss, G. D., Drobny, B., Happer, W., Sauer, K., Springer, S. R., Williams, A., *Nature* **1994**, *370*, 199-201.
- 48 Winkelsch, A. E., Egan, L., Balciunas, D., Johns, F. A., Albert, M. S., *MMR Forum* **2000**, *33*, 245-253.
- 49 Weber, J., Cherepan, A., Gali-Juskas, A., Leach, M., Balciunas, A., *Proc. Natl Acad. Sci. USA* **1999**, *96*, 3664-3669.
- 50 Walsh, R. C., Chopp, T., Coulter, E., Kasser, M., Swanson, S., Agronoff, D., *Nucl. Instr. and Meth. In Phys. Res.* **1998**, *402*, 460-463.
- 51 Song, Y., Gordon, J., Starikov, B., Swart, T., Fourn, A., *J Chem Phys* **1998**, *108*, 6223-6229.
- 52 Fourn, E., Hader, M., Kasser, I., Fourn, A., Rappenstein, I., *J Mag. Res.* **1999**, *176*, 133-139.

73. Møller, B., Chen, X., Charila, M., Deshayes, B., Hoffland, L., Johnson, G., *J Mag Res* **1998**, *127*, 133-140
74. <http://www.physics.fsu.edu/~mshaydip/mshaydip.html>
75. Møller, B., Charila, M., Chen, X., Deshayes, B., Hoffland, L., Whalen, C., Johnson, G., *Magn Res In Med* **1999**, *41*, 1058-1064
76. Bauer, K., Fitzgerald, R., Happer, W., *Chem Phys Lett* **1995**, *233*, 193-198
77. Huska, M., Goodson, B., Lewis, D., Bennett, E., Cyrus, M., Hardin, R., Pines, A., *Chem Phys Lett* **1998**, *293*, 659-660
78. Tang, C., Mao, B., Wang, G., Williamson, D., Cory, D., Walworth, R., *Phys Rev E* **1999**, *59*, 1733-1744
79. Kuzum, H., Sakai, K., Roberts, T., *Eur Radiol* **1998**, *8*, 620-627
80. Deshayes, B., Cohen, G., Miron, E., Sauer, K., Walter, K., Happer, W., *Appl Phys Lett* **1996**, *69*, 1667-1670
81. Fitzgerald, R., Bauer, K., Happer, W., *Chem Phys Lett* **1999**, *304*, 83-87
82. Mao, B., Tang, C., Wang, G., Cory, D., Walworth, R., *Phys Rev E* **2000**, *61*, 0361-0368
83. Back, B., Platt, B., Ornt, S., Thielwoll, P., Salzer, X., Maros, T., Bessmann, H., Seub, M., Cuffin, C., Coudier, S., *MAGMA* **2001**, *13*, 182-187
84. Tang, C., Wang, G., Paneraj, V., Mao, B., Bennett, D., Hoffmann, D., Sauer, K., Norman, F., Cory, D., Walworth, R., *Phys Rev Lett*, **1998**, *80*, 3195-3198
85. Lewis, J., Sauer, K., Coombs, M., *Chem Phys Lett* **2000**, *329*, 359-364
86. Huska, M., Goodson, B., Lewis, D., Bennett, E., Cyrus, M., Hardin, R., Pines, A., *Chem Phys Lett* **1998**, *292*, 689-690
87. Charila, M., Chen, X., Deshayes, B., Fox, D., Happer, W., Sauer, K., *Phys Rev Lett* **1995**, *75*, 490-493
88. Bennett, E., Huska, M., Kuzum, L., Pines, A., Sauer, J., *J Mag Res* **1999**, *138*, 211-219

BIOGRAPHICAL SKETCH

Anthony L. Zook was born in Lancaster, Pennsylvania, on September 3, 1975.

He completed his elementary and high school education in the Mechanics Control School District. He was first introduced to chemistry in the 6th grade by his teacher, Mr. Stuchlik. His interest in chemistry continued to grow in high school, where he completed a summer internship in the laboratory of Prof. Ross Macosko at Franklin and Marshall College. In 1997 Anthony graduated from Franklin and Marshall College with a Bachelor of Arts degree in chemistry. There he performed independent research on glass discharge spectroscopy under the direction of Prof. Ken Hise.

After graduating from F&M, Anthony worked as a Research Scientist for BlackLight Power Inc. There he worked on calibrating and vacuum ultra violet spectroscopy studies of novel chemical reactions. Following one year of employment Anthony enrolled at the University of Florida to pursue a PhD in Chemistry, where he completed his graduate work under the direction of Prof. Ross Brown.

Anthony has been married to Teresa Zook since 1999. He has one daughter, Kaitlyn, born in 2000. Anthony and Teresa are expecting their second daughter in the Fall of 2002.

I certify that I have read this study and that in my opinion it conforms to acceptable standards of scholarly presentation and is fully adequate, in scope and quality, as a dissertation for the degree of Doctor of Philosophy



Clifford B. Brown, Chairman
Associate Professor of Chemistry

I certify that I have read this study and that in my opinion it conforms to acceptable standards of scholarly presentation and is fully adequate, in scope and quality, as a dissertation for the degree of Doctor of Philosophy



James D. Woodward
Graduate Research Professor of Chemistry

I certify that I have read this study and that in my opinion it conforms to acceptable standards of scholarly presentation and is fully adequate, in scope and quality, as a dissertation for the degree of Doctor of Philosophy



William W. Harrison
Professor of Chemistry

I certify that I have read this study and that in my opinion it conforms to acceptable standards of scholarly presentation and is fully adequate, in scope and quality, as a dissertation for the degree of Doctor of Philosophy



Stephen J. Blackburn
Associate Professor of Mathematics

I certify that I have read this study and that my opinion thereon is acceptable in accordance with scholarly presentation and is fully adequate, in scope and quality, as a dissertation for the degree of Doctor of Philosophy



Anthony R. Hoffman
Professor of Materials Science and
Engineering

This dissertation was submitted to the Graduate Faculty of the Department of Chemistry in the College of Liberal Arts and Sciences and to the Graduate School and was accepted in partial fulfillment of the requirements for the degree of Doctor of Philosophy

August 2002

Dean, Graduate School